# First Principles calculation of heavy particle rate coefficients

Richard L. Jaffe[*]
NASA Ames Research Center
Mail Stop 230-3, P.O. Box 1
Moffett Field, CA 94035-0001

David W. Schwenke[†]
NASA Ames Research Center
Mail Stop 258-2, P.O. Box 1
Moffett Field, CA 94035-0001

Marco Panesi[‡]
Department of Aerospace Engineering
University of Illinois at Urbana Champaign
Urbana, IL 61801

December 29, 2014

## 1 Introduction

One important goal of aerothermodynamics research has been understanding the physics and chemistry of shock heated air formed around a space vehicle or object traveling at hypersonic speed through the upper reaches of Earth's atmosphere. The high post-shock temperatures induce chemical changes in the atmospheric gases, *e.g.*, dissociation and ionization, and the low gas density means there are often insufficient collisions between the atomic and molecular species to maintain a state of thermodynamic equilibrium. One consequence of this non-equilibrium condition is an extra amount of photonic emission from the shock layer gas that increases the heat flux impinging on the vehicle.[?] For lunar or mars return missions, the entry velocity will exceed 10 km/s, the shock-layer gases will be mostly dissociated and radiative heating can be a significant contributor to the heat load experienced by the spacecraft. Ground-based shock tube experiments, ballistic range tests and flight tests carried out in the 1960's during development of the Apollo return capsule identified this phenomenon, but could not quantify the extent of this contribution to the total heat flux.[?] Further work in the 1980's to define the requirements for the thermal protection system (TPS) of spacecraft

[*]E-mail: richard.jaffe@nasa.gov
[†]E-mail: david.w.schwenke@nasa.gov
[‡]E-mail: mpanesi@illinois.edu

like the Galileo probe and the Aeroassisted Orbital Transfer Vehicle (AOTV) capsule led to a better understanding of non-equilibrium effects.[?, ?] As computer capabilities increased, NASA began to rely more heavily on Computational Fluid Dynamics (CFD) simulations for space mission design and undertook the development of reacting gas models for CFD to describe re-entry phenomena. The chemical kinetic and multi-temperature models used today by NASA were developed during that time by Chul Park.[?, ?] For that model Park assumed that a single translational or kinetic temperature ($T$) could describe the velocity distribution of all the atoms and molecules and that the vibrational-level population of the molecules is described by a Boltzmann distribution at a different temperature ($T^V$), called the vibrational temperature. Furthermore, it is assumed that vibration and rotation levels are separable and that the rotational level population is described by a rotational temperature ($T^R$) with $T^R = T$ (*i.e.*, the rotational and translational modes are equilibrated). The excited electronic state populations are usually described by a Boltzmann distribution using $T^V$. For the simplified case of a common vibrational-electronic state temperature for all molecules, this is the well-known two-temperature (2-T) model that has been used for non-equilibrium CFD simulations for the last 25 years.[?, ?]

In the 2-T model, the translational temperature $T$ is determined from the overall mass, energy and momentum conservation relationships and $T^V$ is determined from a first-order relaxation equation based on the Landau-Teller equation for the equilibration of a harmonic oscillator:

$$\frac{dE_{vib}(T^V)}{dt} = \frac{E_{vib}(T) - E_{vib}(T^V)}{\tau_{vib}} \tag{1}$$

where $\tau_{vib}$ is the vibrational relaxation time, which is related to the vibrational relaxation rate coefficient ($k(1{\rightarrow}0)$) and $T^V(t)$ is determined by inverting the Boltzmann expression for the thermal vibrational energy:

$$E_{vib} = \sum_v E_{vib}(v) \exp(-E_{vib}(v)/\mathrm{k_B}T^V), \tag{2}$$

where $E_{vib}(v)$ is the energy of the $v^{th}$ vibrational level and $\mathrm{k_B}$ is Boltzmann's constant. The rationale for assuming $T^R = T$ and $T^V < T$ is that, at moderate temperatures (generally $< 5000$ K), the rotational level populations in a gas are equilibrated after a small number of collisions ($\lesssim 10$), while equilibration of the vibration populations require $\approx 10^3$ collisions. Data for parameterizing rotational and vibrational relaxation times have generally come from shock-tube experiments at temperatures of 5000-10,000 K, and usually are extrapolated to 20,000 K or even higher. However, at temperatures greater than 10,000 K vibration and rotation relaxation times are comparable and a coupled rotation-vibration relaxation model is a more accurate description. For a harmonic oscillator (*i.e.*, the original Landau-Teller model), collisions can only change the vibrational quantum number by $\Delta v = \pm 1$, so the equilibration occurs by a series of small steps. In reality, however, owing to effects of anharmonicity and chemical reactions, larger $\Delta v$ are likely. Park also defined an average temperature,

$$T_{ave} = T^p {\times} T^{V^{(1-p)}}, \tag{3}$$

(originally $p = 0.5$ was used so $T_{ave}$ was given by $\sqrt{T{\times}T^V}$) and modified the familiar Arrhenius expression for the collisional dissociation reaction rate coefficient by using $T_{ave}$ instead of $T$

$$k^D(T_{ave}) = AT_{ave}^n \exp(-T_d/T_{ave}), \tag{4}$$

2

where $A$ is the pre-exponential constant, $n$ is the temperature coefficient and $T_d$ is the dissociation temperature $(D_0/(N_{av}k_B))$. $D_0$ is the dissociation energy and $N_{av}$ is Avogadro's number $(6.0225\times10^{23}$ atoms or molecules per mole). Usually $T_d$ is fixed at the experimental value while $A$ and $n$ are treated as adjustable parameters.

The treatment of vibrational relaxation and the use of $T_{ave}$ in the 2-T chemistry model create a time delay for dissociation that approximates the induction time observed in shock tube experiments, while still allowing for some some rapid atom production behind the shock. In shock tube experiments for gas mixtures that include $N_2$, the initial radiation pulse is due to $N_2$ 1st positive transition. The Arrhenius pre-exponential factor $A$ and the temperature coefficient $n$ were adjusted so the computed non equilibrium emission matched the observed experimental quantity. A more detailed discussion of the collisional physical and chemical processes and the implementation of the 2-T model is given in Park's textbook "Non equilibrium Hypersonic Aerothermodynamics".[?] The framework of the 2-T model is essentially empirical, because the *ad hoc* definition of $T_{ave}$ and some of the individual reaction rate coefficient parameters were adjusted so the CFD calculations of the flow behind a shock could reproduce a set of experimental observations. As newer experimental data became available, more empirical adjustments have been made.[?, ?]

A full characterization of the non equilibrium gas requires detailed accounting of the distribution of rotation-vibration levels and electronic states for each of the air species. When the 2-T model was being developed, such an undertaking was completely impractical. With current computational resources that is no longer the case and a group of scientists at NASA Ames Research Center has begun the task of formulating a detailed collisional model for hypersonic flows. This new high-fidelity air chemistry model is based on first principles theoretical calculations that will be suitable for Earth entry at velocities of 10-15 km/s and Mars entries at velocities up to 8 km/s. It has long been realized that computational chemistry modeling can be used to determine the dissociation and energy transfer rates for high-temperature air under these conditions. The atomistic simulation methods for studying these collisional processes are based on classical mechanics, but require knowledge of the inter-atomic forces acting between the collision partners, which can be obtained from the change in the total potential energy during a collision. The potential energy surface (PES) is the representation of the total potential energy of the system at all geometric arrangements of these collision partners and the inter-atomic forces are the negatives of the derivatives of PES with respect to the geometric coordinates. Originally, empirical potential energy surfaces, with parameters that had been adjusted to reproduce available experimental data,[?] were used for the PES. For example, Billing,[?] Lagana[?, ?] and Esposito[?] and their coworkers have used this approach, coupled with classical or semi-classical scattering calculations for computation of collision cross sections and dissociation rate coefficients for $N_2 + N$ collisions. However, with current computer resources, it is possible use *ab initio* quantum chemistry methods to compute the potential energy of the atoms and molecules involved in the collision for a large number of geometric arrangements. An analytical representation of the resulting potential energy surface (PES) can be combined with a classical scattering method called quasi-classical trajectory (QCT) for the simulation of large numbers of collisions to obtain collision cross sections and reaction rate coefficients. As part of our work, we have computed complete sets of cross sections and state-specific rate coefficients for rotation-vibration energy transfer and dissociation in collisions of $N_2 + M$, where M = N or $N_2$. For $N_2 + N$ these data have been used to evaluate the relaxation and excitation rates for all rotation-vibration energy levels of $N_2$ to enable us to fully characterize the shock layer for air under hypersonic conditions. The goal of this project is to construct a hypersonic chemistry model for non-equilibrium flows that is free from assumptions about temperatures. This project was started with support of

the NASA/ARMD Fundamental Aerodynamics Program and is currently sponsored by the Entry Systems Modeling project in the NASA Space Technology Mission Directorate (STMD).

In this chapter we illustrate the computational methods used for computing detailed energy transfer and dissociation rate coefficients for $N_2$ + N and $N_2$ + $N_2$ collisions. In section 2 we describe the methods used for quantum mechanical calculation of potential energy surfaces and the analytical representation of the PES used in the quasi-classical trajectory calculations and in section 3 we describe the QCT method and present some of the rate coefficients that we obtained from of those calculations. In section 4 we describe a master equation model that uses the detailed rate coefficients to determine phenomenological reaction rates at conditions appropriate to hypersonic flows and a coarse grained model to generate a reduced set of rate coefficients that can be used for CFD simulations. Our goal for this chapter is to demonstrate some of the approximations and trade-offs that must be made to make this endeavor feasible with current computer resources.

Before starting to describe the specific methods we have been using, we provide justification for our hybrid quantum/classical approach. The determination of the state-to-state cross sections and microscopic rate coefficients required to describe the dissociation/excitation/relaxation processes via first principles requires the description of the behavior of three or four nitrogen nuclei and 21 or 28 electrons for $N_2$ + N and $N_2$ + $N_2$ collisional processes, respectively. This is a very complicated problem, and approximations are required to make progress. Fortunately, over the last many decades, procedures that yield reliable results have been developed.

One problem is that, in contrast to our macroscopic world, the world of atoms and molecules is very different. This is primarily due to their relative sizes. Calculations of atomic and molecular properties are most conveniently carried out in atomic units, and in the system of units we use, Hartree atomic units, the unit of length is the Bohr radius $a_o$, the unit of mass is the electron mass $m_e$, the unit of charge is the electron charge $e$, and Planck's constant $h$ is taken to be equal to $2\pi$, or rather $\hbar = h/2\pi = 1$. In more customary units, 1 $a_o \approx 0.53 \times 10^{-10}$ m, 1 $m_e \approx 9.1 \times 10^{-31}$ kg, 1 $e \approx 1.6 \times 10^{19}$ C, and $h \approx 6.6 \times 10^{-34}$ J-sec. Planck's constant governs the degree of quantum behavior via the dimensionless ratio of the De Broglie wavelength $\frac{h}{p}$ to characteristic size of the system, where the momentum $p$ is most conveniently expressed in terms of the energy: $E = p^2/2m$, where $m$ is the mass of the system. If we are considering an electron near a nitrogen nucleus, taking $E$ to be the ionization potential, 14.5 eV, so that $p \approx 1$ atomic unit, and the characteristic size to be the equilibrium bond length of the ground state of $N_2$ divided by 2, $i.e.$ 2.06 $a_o/2 \approx 1$ $a_o$, this ratio is equal to $2\pi$. If we are considering a nitrogen nucleus, $m \approx 2.5 \times 10^3$ $m_e$ and if we take $E = k_B T$, where $k_B$ is Boltzmann's constant (in Hartree atomic units $k_B \approx 3.2 \times 10^{-6}$), then at T = 10,000 K we find $p = 40$ a.u. Taking the characteristic length be $\approx 10$ $a_o$ gives us a dimensionless ratio of $1.6 \times 10^{-2}$. In comparison, a macroscopic object like a baseball traveling at 94 mph (42 m/s), such as a fast ball thrown by a major leaguet pitcher, has $p = 3.0 \times 10^{24}$ a.u. Taking the characteristic length to be 1 meter, the dimensionless ratio is $1.1 \times 10^{-34}$. The for an electron, a nitrogen atom and a baseball the De Broglie wavelengths are approximately 6.3, $10^{-2}$ and $10^{-34}$, respectively.

It is thus seen that although an electron is very clearly quantum mechanical in nature and a baseball is very clearly governed by classical mechanics, the motion of an atom or small molecule is somewhat intermediate in nature. There are many aspects of nuclear motion that are well described by classical mechanics, while others, like sub-threshold tunneling and pre-dissociation, as well as nuclear spin symmetry, arise purely from quantum effects. The set of approximations that we use is to formulate the problem in terms of quantum mechanics, but then substitute classical mechanics where it is applicable. To simulate some phenomena, we must resort to "semi-classical" or "old quantum mechanics" treatments, and this will be discussed in detail below.

# 2 Calculation of Potential Energy Surfaces

In quantum mechanics, the interactions between the particles (*e.g.*, atomic nuclei and electrons) is given by the time-dependent Schrödinger equation:

$$i\hbar\frac{d}{dt}\Psi(x,t) = \left[-\frac{1}{2}\nabla^2 + V(x)\right]\Psi(x,t) = H(x)\Psi(x,t), \tag{5}$$

where $\Psi$ is the wave function, $H$ is the Hamiltonian operator that governs the total energy (i.e., kinetic plus potential energy $V$). For conservative systems, $H$ and $V$ only depend on the position coordinates, $x$, and the wave function can be factored into time-dependent and time-independent components, $[\exp(-iEt/\hbar)]$ and $[\psi(x)]$, respectively. The resulting time-independent Schrödinger equation,

$$H(X)\psi(x) = E\psi(x), \tag{6}$$

is used to compute the state energy of the particles in a stationary state.

The first approximation we make to enable a practical solution is to invoke the Born-Oppenheimer approximation[?] to separate the electronic and nuclear motion. We justify this by the low density of electronic states and very large mass difference between an electron and a nitrogen nuclei - as mentioned above that ratio is about $2.5 \times 10^3$. The low density of states means that we can just consider one electronic state, and the mass ratio means we can neglect the action of nuclear momentum operators on the electronic wave function. Under these conditions, the equations of motion for the nuclei are equivalent to the classical motion of three or four nitrogen atoms on a potential energy hyper-surface (PES) in 9 or 12 dimensions, and the height of this surface is given by the sum of the electronic energy and nuclear potential energy calculated at a given geometry of the nitrogen nuclei.

At this point, it is worth while to discuss the coordinates that are used in this work. The motion of the electrons is very strongly coupled to the positions of the nuclei, and since the nuclei are taken to move slowly compared to the electrons, we use cartesian coordinates for the electrons, and the origin of this coordinate system will be the center of mass of the nuclei.

For the nuclei, we will use a variety of coordinate sets. Starting from the $3 \times 3 = 9$ cartesian coordinates of the atoms, we can transform to a set of relative coordinates whereby $3 \times 2 = 6$ coordinates specify the nuclear positions relative to the nuclear center of mass, and 3 coordinates specify the center of mass. We will consider two sets of relative coordinates. This first is called Jacobi coordinates, and they consist of the vector $\mathbf{r}_a$ that goes from the position of $N_a$ to the center of mass of $N_bN_c$, and the vector $\mathbf{R}_a$ that goes from the position of $N_b$ to the position of $N_c$. The spherical polar form of these vectors are particularly useful in describing situations where $N_a$ is far from $N_bN_c$. We define in a cyclic fashion the vectors $\mathbf{r}_b$, $\mathbf{R}_b$ and $\mathbf{r}_c$, $\mathbf{R}_c$. Thus we see that for the case of the reaction $N_a + N_bN_c \rightarrow N_b + N_cN_a$, we would want to start out using $\mathbf{r}_a$ and $\mathbf{R}_a$ and end up using $\mathbf{r}_b$ and $\mathbf{R}_b$. This is indeed what one does if quantum calculations are carried out. However in the classical calculations, it is not at all convenient to change coordinates during the course of a trajectory. While in principle, one could use say $\mathbf{r}_a$ and $\mathbf{R}_a$ for the reactive collision, but after the reaction, both vectors would become large as the products separated from each other, and one could have numerical problems converting into the more physical coordinates. Thus when we carry out our classical trajectories, we use cartesian coordinates for the first two atoms, and determine the coordinates for the third atom by requiring that the center of mass be at the origin.[?][?]

The Jacobi coordinates can be converted from cartesian to spherical polar coordinates: $i.e.$ $\mathbf{r}_a$ can be parameterized by $r_a$, $\theta_a$, and $\phi_a$, etc. Another useful parameterization is to transform to a rotating coordinate system whereby the Jacobi coordinates take the form

$$\left(\mathbf{r}_a \mathbf{R}_a\right) = \begin{pmatrix} 0 & R_a \sin \chi_a \\ 0 & 0 \\ r_a & R_a \cos \chi_a \end{pmatrix}. \tag{7}$$

Then the complete set of coordinates are $r_a$, $R_a$, $\chi_a$, $\alpha_a^{LB}$, $\beta_a^{LB}$, and $\gamma_a^{LB}$, where the last three angles are the Euler angles that take the rotating system to the non-rotating system.[?][?]

When representing potential energy hyper-surfaces for 3- and 4-atom systems, like $N_3$ and $N_4$, it is convenient to use the three or six atom-atom distances $R_{ij}$, respectively. These coordinates, however, are not suitable for dynamics calculations, because they are not all independent, $i.e.$

$$R_{ab} \leq R_{ac} + R_{bc}. \tag{8}$$

However, it is quite easy to use them with the law of cosines to generate the other internal coordinates.

The potential energy hyper-surface is a function of 3n-6 geometric coordinates and represents the potential energy for all geometric arrangements of the n atoms comprising the colliding species. Note that in this treatment the position of the center of mass of the system and its orientation with respect to the center of mass are considered stationary. For atom-diatomic molecule collisions ($e.g.$, $N_2$ + N) n = 3 and the PES is a function of 3 positional variables. For collisions between two diatomic molecules, n=4 and the PES is a 6-dimensional hyper-surface. We obtain the PES by solving the time-independent Schrödinger equation for the energy of the electrons with the nuclei fixed at some geometric arrangement. The quantum Hamiltonian operator H consists of a electron kinetic energy term and coulomb potential terms for electron-electron and electron-nuclei interactions. The resulting electronic energy E is the value of the potential energy of atoms at that geometry. The wave-function $\psi$ contains information about the probability density distribution of the electrons in the presence of the nuclei. For all but the simplest cases, the electronic Schrödinger equation is solved by a series of numerical expansions. First, the wave function taken to be a linear combination of hydrogenic atomic orbitals, each expressed as a sum of Gaussian functions centered on each nucleus (called the one-particle basis set). Then the electron-electron coulomb potential is simplified so each electron experiences only the average potential of the remaining electrons (the so-called Hartree Fock approximation) and the Schrödinger equation is solved variationally to minimize the energy E. The resulting coefficients for the basis transform the atomic orbitals into molecular orbitals that are delocalized over all the nuclei. To go beyond the Hartree Fock approximation, electron correlation effects are considered whereby each electron feels the instantaneous potential of the other electrons. Electron correlation is usually introduced by mixing in a series of arrangements of electrons in the molecular orbitals (a second expansion over molecular orbitals) and solving the resulting eigenvalue problem. It is generally not possible to obtain the exact solution of the electron correlation contribution to the total energy for a given atomic orbital basis, because the number of arrangements in the molecular orbitals grows factorially with the number of electrons. Thus, numerical methods have been devised to obtain the bulk of the electron correlation energy in the most economical fashion.

For $N_2$ ($X^1\Sigma_g^+$) + N ($^4S$) collisions, we need to compute the ground electronic state energy for $N_3$, which has quartet electronic spin multiplicity and $A$" symmetry (denoted $^4A$"). If the three N atoms are labeled $N_a$, $N_b$ and $N_c$, the PES describes the $N_aN_b$, $N_aN_c$ and $N_bN_c$ nitrogen molecules, separated atoms ($N_a$ + $N_b$ + $N_c$) and a possible triatomic complex ($N_aN_bN_c$ and its

permutations). If we consider the collision between $N_a$-$N_b(v, J)$ and $N_c$, the possible outcomes are $N_a$-$N_b(v', J')$ + $N_c$, $N_a$-$N_c(v', J')$ + $N_b$, $N_b$-$N_c(v', J')$ + $N_a$, and $N_a$ + $N_b$ + $N_c$. The first outcome is a nonreactive, but inelastic, collision resulting in the $N_2$ molecule having a different internal energy level and the last is dissociation of the initial $N_2$ molecule. The other two outcomes represent products of an exchange reaction where the atoms comprising the final $N_2$ molecule are different from the initial molecule. This PES is a function of three geometric variables (the atoms form a triangle defined by the three N-N inter-nuclear distances or two N-N inter-nuclear distances and one angle). For a 4-atom system like $N_2$-$N_2$, the situation is considerably more complicated. Six geometric variables are required to define the arrangement of the atoms and there are three different pairs of $N_2$ molecules that can be formed.

Many computer codes are available to carry out *ab initio* electronic structure calculations. We use a modified version of MOLPRO.[?] Most utilize the same basic numerical methods for solving the electronic Schrodinger equation. In our opinion, Molpro is a very efficient code for calculating the sophisticated electronic wave functions and energies required for the determination of a complete PES for a three- or four-atom system. For this work, we use the augmented-correlation consistent polarized valence triple zeta (aug-cc-pVTZ) one-particle basis set of Dunning.[?] The correlation consistent polarized valence basis sets are a family of basis sets that systematically improve the accuracy of the expansion. The double zeta set has 3 $s$-type, 2 $p$-type and 1 $d$-type functions centered on each nitrogen atom. Triple zeta as has 4 $s$-type, 3 $p$-type, 3 $d$-type and 1 $f$-type functions, and so on. These sets can be augmented by adding more diffuse basis functions for more flexibility in describing the electron distribution around the nuclei when the bonds are stretched. The aug-cc-pVTZ basis set consists of 5 $s$-type functions, 4 $p$-type functions, 3 $d$-type functions, and 2 $f$-type functions centered on each nitrogen nuclei. There are a total of 138 basis functions, and this represents a compromise between the 'good' correlation consistent valence triple zeta one-particle basis set of Dunning[?] and the 'better' correlation consistent valence quadrupole zeta one-particle basis set of Dunning.[?] The Dunning basis sets are the current *de facto* standard for this type of electronic structure calculations.

An earlier version of the $N_3$ PES was published in 2003[?] in which we were mainly concerned about the potential energy hyper-surface in the vicinity of the reaction path for the nitrogen exchange reaction, *i.e.* the most important region for the process $N_a$+$N_bN_c \rightarrow N_b$+$N_cN_a$. To study the dissociation reaction as well, we decided to recompute the entire PES using a different approach to solving the electron correlation problem. This newer PES is described in .[?, ?] Galvao and Varandas[?] have also computed the $N_3$ ($^4A"$) PES using a similar approach. Our $N_4$ PES has been described in Refs. [?, ?]. All of these PES calculations utilized the same aug-cc-pVTZ one-particle basis set, but the details of the methods used to compute the electronic energies are somewhat different.

More recently, Paukku *et al.*[?] have carried out calculations on the $N_4$ system, and they also used a one electron basis set based on the the cc-pVTZ basis, except that they augmented the basis only with diffuse $s$ and $p$ type functions, whereas in the aug-cc-pVTZ basis, diffuse $d$ and $f$ functions are also added. In our work, we used the full set of diffuse functions for several reasons. First of all, convergence tests[?] show that the rate of convergence of the fully augmented basis sets is superior to the un-augmented ones, and just including $s$ and $p$ functions would reduce the convergence rate to be the same as the un-augmented basis sets. Secondly, one of the purposes of augmenting the basis with diffuse functions is to gain a better description of the outer reaches of the molecular orbitals. This is important, for the asymptotic dependence of the molecular orbital on radial distance is a decaying exponential, while the basis functions have a Gaussian form which

decays much faster. Thus we expect that as the diatom dissociates, there will be intermediate regions where the potential energy is transitioning from the non-interacting region to the strongly interacting region where the results might be quite sensitive to the outer reaches of the basis. This is an effect that might change the shape of the potential energy hyper-surface and hence impact the dissociation rate, but not have significant effect on the properties near the equilibrium bond length and the dissociation energy. There is no particular reason to suppose that this effect is limited to only $s$ and $p$ symmetries. The third reason is nitrogen is a rather odd atom. Specifically, it has no bound anion states, yet in the presence of other atoms, it tends to play roles that indicate electron affinity. For example, the dipole moment of $NH_3$ is substantial and the CN group is a notorious electron withdrawing group in organic compounds. Another role of the diffuse functions is to help with the description of anionic character in the wave function. This dichotomy, coupled with the fact that the exponential parameters in the basis sets are optimized solely for the ground electronic state of the atom, tends to bias the calculations towards further soft pedaling of any ionic character. See [?] for an indication of this. Thus we believe our choice of basis is superior to that of Paukku *et al.*

For our initial calculations[?], we determined the MOs via the spin-restricted Hartree-Fock (RHF) approximation, and then determined the electronic energy using the spin-unrestricted coupled-cluster single-doubles (UCCSD) approach with the (T) correction. In these calculations, the $1s$-like MOs were always kept doubly occupied, and we computed the electronic wave functions for the lowest energy quartet $A''$ state. This is the spin-space symmetry that includes the ground state of $N_2$ (X $^1\Sigma_g^+$) + N($^4S$).

While the RHF UCCSD(T) calculations are an efficient way of computing good approximations for the electronic energy in the vicinity of the reaction path for the nitrogen exchange reaction, the assumptions explicit in the method break down when an collision results in dissociation, and non-physical energies would be obtained.

Thus, in order to be able to accurately treat dissociative collisions, we need to go to more sophisticated methods. This is because although the electronic wave function for $N_2$ X $^1\Sigma_g^+$ near its minimum energy geometry is reasonably well described by a zero order function that only includes closed shells, *i.e.* where all MOs are doubly occupied, at the dissociation limit, the electronic wave function requires a zero order function that includes at minimum six open shells, *i.e.* half filled molecular orbitals. But the RHF method requires a fixed number of open and closed shells, so can not make a smooth transition from closed to open shells.

The methods required to smoothly treat variable number of open shells all start with the multi-configuration Hartree-Fock (MCHF) method to determine the MOs. In the MCHF calculations, the number of occupied orbitals are increased compared to the RHF method, and in the determination of the MOs, we also simultaneously determine configuration mixing coefficients. In the RHF calculations, there is no configuration mixing. This makes the MCHF calculations much more expensive, but it also makes them much more robust in being able to reasonably describe an infinite gradation of bonding possibilities.

Once we have the MOs from the MCHF calculations, we consider two ways to compute the electronic energy. In the first method, the internally-contracted Multi-reference-configuration-interaction (icMRCI) method, we diagonalize the electronic Hamiltonian in a very large basis (upwards of tens of millions of functions) of configuration state functions. The icMRCI method is a very general method, capable of giving very good energies and wave functions for very general situations, but at the cost of being significantly more expensive than the UCCSD method. In the second method, we used the internally-contracted Average-Coupled-Pair-Functional (icACPF)

method. This method is of very similar cost to the icMRCI method, but improves the treatment of electron rich systems. The trade-off, however, is one can only get results for the lowest spin-symmetry state, and one only gets an energy but not a wave function. The icMRCI energies can also be simply improved somewhat by using the Davidson quadrupoles correction (+Q), and we will do so in our calculations. Which energy, ACPF or icMRCI+Q, is better is a matter of debate.

In our original plan of attack, we were going to augment our previously determined RHF UCCSD(T) energies at 4306 geometries with MCHF icMRCI+Q energies computed in the dissociation regime. Thus we carried out MCHF icMRCI+Q calculations at 56 geometries. In these calculations, we also used the aug-cc-pVTZ one particle basis, while in the MCHF calculations, we included three doubly occupied MOs and 15 electrons in 12 active MOs, and optimized the MOs and configuration mixing coefficients by minimizing the energy of the lowest quartet $A''$ state. In the icMRCI+Q calculations, we kept the 3 N $1s$-like MOs doubly occupied, but correlated the remaining 15 electrons, again going after the lowest quartet $A''$ state. These calculations were very expensive, and as it turned out, not useful. This is because as $N_2$ dissociates, the configuration mixing coefficients lead to the $2s$- like MOs being only doubly occupied. This then means that the MCHF energy becomes only very weakly dependent on mixing between the $1$-$s$-like MOs and the $2$-$s$ like MOs. Then since the $1s$ and $2s$-like MOs are not treated the same in the icMRCI calculations, erratic results were seen in the final energies. The resolution of this problem that we used was to change to a MCHF calculation where we included six doubly occupied MOs and 9 electrons in 9 active MOs. However we still correlated the $2s$-like MOs in the icMRCI+Q calculations. This made the energies much more reliable and also reduced the cost somewhat. However, these calculations were still quite arduous not only because of the large number of variables that must be optimized, but also because the variation of the number of open-shells from three to nine severely tested the numerical schemes in MOLPRO. Thus we also investigated the effect of not correlating the $2s$-like MOs in the icMRCI calculations.

As a test of this approximation compared to the icMRCI+Q calculations correlating 15 electrons, we carried out the analogous calculations on the X $^1\Sigma_g^+$ state of the $N_2$ molecule. The results are shown in Fig. 1. For $N_2$, the analog of the RHF UCCSD(T) calculations are the HF CCSD(T) calculations, the analog of the 15e icMRCI+Q calculations are the 10e icMRCI+Q calculations, and finally the analog of the 9e ACPF calculations are the 6e icACPF calculations. We also show the results using the aug-cc-pVTZ basis and 6e CASPT2 energies, which is the equivalent to the calculations of Paukku[?] as well as the accurate experimentally determined curve of LeRoy *et al.*[?] All curves are shifted to have the zero of energy at the equilibrium bond length. At the level of resolution of this figure, energies from the icMRCI, icMRCI+Q, and ACPF methods are indistinguishable. We see that near the minimum, all three curves are indistinguishable, with the HF CCSD(T) results diverging from the the 10e icMRCI+Q results starting about 3 $a_o$, and the 6e icACPF tracking the 10e icMRCI+Q results very well out to the dissociation limit. The principle difference between the 6e and 10e calculations are the 6e results give a little larger dissociation energy, and this in fact greatly improves the agreement with LeRoy's potential. This is of course due to fortuitous cancellation of error, but it appears that either calculation does a pretty good job of prediction the potential curve. The 6e icCASPT2 results track the 6e icMRCI+Q results quite well until about 3.5 $a_o$, after which they behave in somewhat an erratic manner.

It is interesting to consider what sort of calculation is required to do a better job on the $N_2$ potential curve. In Fig. 2, we show the results of a sequence of three calculations of $V^{NN}$ compared to the LeRoy potential. In these calculations, we determined the MOs using 6 electrons in the active space, but then when we determined the energies, we correlated all the electrons. The three
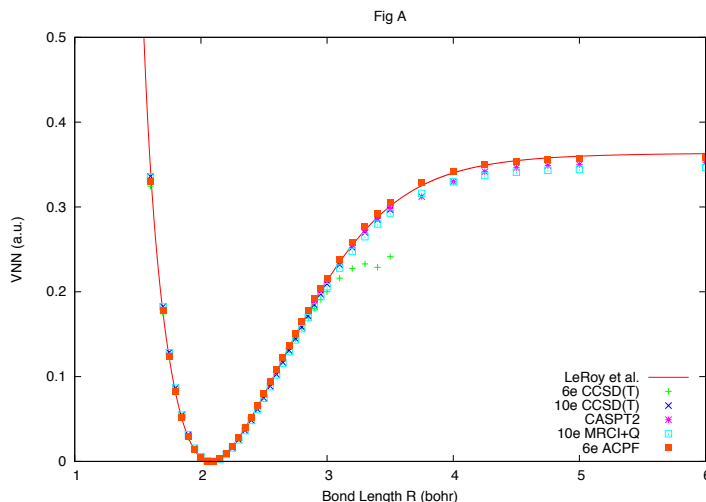
Figure 1: Potential energy curves for $N_2$. $V^{NN}$ has atomic units (i.e., au or hartree).

calculations differ in they used the *spdf*, *spdfg*, and *spdfgh* core-valence basis sets recommended by Schwenke.[**?**] One can see these calculations are nicely converging to a dissociation energy very close to that given by LeRoy's empirical potential. Because of the larger one-electron basis sets used, and the fact that all electrons are correlated, calculations at the *spdfgh* level are currently not feasible for the $N_3$ potential energy hyper-surface.

Thus in the icMRCI+Q calculations for $N_3$, we will only correlate 9 electrons.

When we attempted to construct an analytic representation based on the composite RHF UCCSD(T) and MCHF icMRCI+Q energies, we did not obtain very reasonable results. More icMRCI+Q data was added, eventually up to 421 geometries, and high energy RHF UCCSD(T) energies were deleted, all to no avail. Finally this was eventually traced back to erratic behavior of the RHF UCCSD(T) energies, probably due to the RHF calculations converging to local minima rather than the global minimum. After multiple failed attempts to correct this situation, we decided to discard the RHF UCCSD(T) energies and carry out new calculations.

The most consistent approach would have been to carry out additional icMRCI+Q calculations. However, due to a variety of reasons, we instead used the 9e icACPF method for the replacement points. Using this method, we computed energies at 923 different geometries. These geometries were a mixture of densely spaced points near the transition state geometry for the exchange reaction as well as a uniform grid in $R_{ab}$, $\theta_{abc}$, and $R_{bc}$. Altogether, the icMRCI+Q calculations were based on a grid having $\theta_{abc} = 70, 90, 120, 150,$ and 175 degrees, $R_{ab} \leq R_{bc}$ with values taken from 3,3.25,3.5,3.75, 4, 4.5, 5, 5.5, 6, 7, 8, 9, and 10 bohr. In the ACPF calculations, we augmented the $\theta_{abc}$ values listed above with 70, 80, 100, 110, 116.5, 130, and 165 degrees, and used $R_{ab} \leq R_{bc}$ with $R_{ab}$ taken from 1.6, 1.7, 1.8, 1.9, 2,2.15, 2.3, 2.5, 2.8, and 3 bohr, and $R_{bc}$ sampling those as well
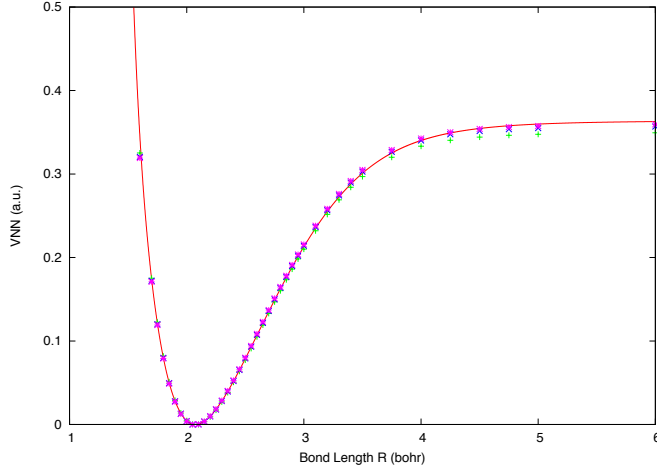
Figure 2: Potential Curves for $N_2$ correlating all electrons: line LeRoy potential, $+$ *spdf* basis, x *spdfg* basis, and finally the *spdfgh* basis

as 3.5, 4, 5, 6, 8, and 10 bohr.

Now we can not directly mix the 9e MCHF icACPF and 9e MCHF icMRCI+Q energies, because although the change in the method of computing the energies does not significantly alter the shape of the potential energy hyper-surface, it does change the height of the potential energy hyper-surface. Before we carried out the determination of the parameters in the analytic representation, we corrected the energies to make them compatible. Specifically, we took the PES to take the form

$$V = V^{\text{NN}}(R_{ab}) + V^{\text{NN}}(R_{bc}) + V^{\text{NN}}(R_{ac}) + V^{3-\text{body}}(R_{ab}, R_{bc}, R_{ac}), \qquad (9)$$

where $R_{ij}$ is the distance between nuclei $i$ and $j$ and $V^{\text{NN}}$ is the asymptotic $N_2$ X $^1\Sigma_g^+$ potential curve, and then we assumed that although $V$ and $V^{\text{NN}}$ will be different for the 9e MCHF icACPF and 9e MCHF icMRCI+Q calculations, $V^{3-\text{body}}$ will be the same, apart from a constant. We will address this assumption later.

Thus in the course of the is work we determine three different $N_2$ X $^1\Sigma_g^+$ potential curves. The first is a fit to 6e MCHF icACPF data, shifted to match the asymptotic 9e MCHF icACPF data, the second is a fit to the 6e MCHF icMRCI+Q data, shifted to match the asymptotic 9e MCHF icMRCI+Q data, and the final one is based on a fit to extensive experimental data.[?] The first two $V^{\text{NN}}$ functions were only used in the fit to determine the parameters in $V^{3-\text{body}}$, while the third $V^{\text{NN}}$ function was used only in the final PES.

In preliminary calculations, we directly used the LeRoy $V^{NN}$ as the third function. However it soon became apparent that in some regions, our potential had non-physical energies. Part of these were traced by to non-physical behavior of the LeRoy potential curve: the short range repulsive part of the potential was much, much too strong. That this occurred is perhaps not to surprising,

11

for the experimental data used to refine that function is not sensitive to that part of the potential. Thus we re-fit the LeRoy potential with the same functional form as we used for the *ab initio* data, but only used points generated from the LeRoy potential below the dissociation limit.

The functional forms used were as follows: we write $V^{NN}$ as the sum of a long range term, a repulsive term, and a short range term. The long range term takes the form

$$-\frac{C_6}{R^6 + \delta^6} - \frac{C_8}{(R^4 + \delta^4)^2} - \frac{C_{10}}{(R^2 + \delta^2)^5},$$
(10)

the repulsive term being

$$49\exp(-\alpha_r R)/R,$$
(11)

and the short range term being

$$R^6\exp(-\alpha_s R)\sum_j C_j(R - R_e)^j.$$
(12)

The values of $C_n$ in the long range term were taken from, the sum over $j$ in the short range term running over $j = 0 - 7$, the exponent 6 was chosen by trial and error, and the $C_j$, $\alpha_r$, $\alpha_s$, and $\delta$ were determined by a nonlinear least squares fit.

Now we further decompose $V^{3-\text{body}}$ into long range and short range interactions:

$$V^{3-\text{body}} = V^{LR}(R_c, r_c, \theta_c) + V^{LR}(R_a, r_a, \theta_a) + V^{LR}(R_b, r_b, \theta_b) + V^{SR}(R_{ab}, R_{ac}, R_{bc}),$$
(13)

where $\mathbf{r}_c$ is vector from $N_c$ to the average of the $N_a$ and $N_b$ positions, $\mathbf{R}_c$ is the vector from $N_a$ to $N_b$, $r_c$ is the length of $\mathbf{r}_c$, $R_c$ is the length of $\mathbf{R}_c$, and $\theta_c$ is the angle between $\mathbf{r}_c$ and $\mathbf{R}_c$, *etc*. For the long interaction we use[?]

$$V^{LR} = -C_6 P_2(\cos\theta)\exp\left[-a^{LR}(R - R^{LR})\right]/(r^6 + r_d^6),$$
(14)

where $P_l$ is a Legendre polynomial, and the parameters $C_6$, $a^{LR}$, $R^{LR}$, and $r_d$ determined from previous work on $N_2+N$ transport properties(REF?).

The short range term is given by

$$V^{SR} = \sum_\alpha \exp(-b_1 r_\alpha^2 - b_2 R_\alpha^2)\sum_{ijk} C_{ijk} r_\alpha^i R_\alpha^j P_k(\cos\theta_\alpha),$$
(15)

where $\alpha = a, b$, or $c$, and the parameters being optimized by fitting to the *ab initio* data were $b_1$, $b_2$, and the $C_{ijk}$.

We experimented with several choices for the limits on the $ijk$ sum, and settled on the terms with $k$ even and $0 < i + j + k \le 7$, excluding the terms with $ijk = 000, 100, 010, 200$, and $020$. This lead to 52 terms.

We optimized the fitting parameters via weighted non-linear least squares. The weights $w$ were taken to be

$$w = 1 + a_w \sum_\alpha \exp\left[-a_R(R_\alpha - R_{ts})^2 - a_\theta(\cos\chi_\alpha - \cos\chi_{ts}) - a(\tilde{R}_\alpha - \tilde{R}_{ts})^2\right],$$
(16)

where $\tilde{R}_a = R_{ab}$, $\chi_a$ is the *abc* angle, with cyclic permutations defining the other quantities. The variables sub-scripted *ts* are those corresponding to our estimate of the transition state geometry

12

for the exchange reaction. This term ensures that our analytic representation faithfully represents the region of the transition state, for $a_w = 25$.

Despite all our efforts to use only reliable input *ab initio* data in the determination of the analytic representation, bad points can occur. This might be due to the MCHF calculations not converging to the global minimum, or it might by due to an excited electronic state crossing the state we are interested in. At any rate, it is important to be able to identify these points and not include them in the final determination of the fitting parameters. We did this as follows. We started out using the weights given above, and performed a non-linear least squares fit. Then we computed the percentiles of the error distribution. If the error at a given geometry was over 5 times the 90'th percentile, or more negative than 5 times the error of the 10'th percentile, then the weight for that point was zeroed, and the parameters were re-fit. We then iterated this until no more points were eliminated. In our final fit, 28 points of the 1344 total had their weights set to zero.

Using this function we then looked at the properties of the exchange reaction transition state region of the PES. This region is characterized by a local energy minimum for equal equal $N_a$-$N_b$ and $N_b$-$N_c$ bond lengths and an $N_a$-$N_b$-$N_c$ bond angle of $\approx 120^{\circ}$ and energy barriers for dissociation of the $N_3$ complex into $N_a$-$N_b$ + $N_c$ and $N_a$ + $N_b$-$N_c$. The energy minimum has traditionally been dubbed "Lake Eyring", in honor of Henry Eyring who formulated the first practical theory of chemical reaction rates. First of all, we consider our purely *ab initio* potential energy surface, *i.e.* we use for $V^{\mathrm{NN}}$ the fit to the 6e icACPF data. The predicted barrier energy is 55.3 kcal/mol, and the predicted Lake Eyring minimum is 52.9 kcal/mol above the energy of separated $N_2$ and N. This is about 10 kcal/mol higher than our previous predictions.[?] Now if replace the *ab initio* $V^{NN}$ with the one based on LeRoy's potential,[?] the transition state energy is now predicted to be 45.5 kcal/mol and Lake Eyring minimum to be at 43.5 kcal/mol. This is in quite good agreement with our previous calculations correlating 15 electrons. The N-N bond lengths and bond angle for the barrier geometry are 1.18 and 1.46 A (2.23 and 2.75 bohr, respectively) and $120^{\circ}$. For Lake Eyeing the bond length is 1.26 A (2.38 bohr) and the bond angle is $119^{\circ}$. Galvao and Varandas[?] report similar geometries and energies for their $N_3$ PES. Our PES is shown in Fig.. The internal lines in the figure represent equal energy contours. The closed loops under the label $N_a N_b N_c$ is Lake Eyring, the dark blue regions represent the reactants and products of the exchange reaction and the plateau with the label $N_a$+$N_b$+$N_c$ represents the dissociation products.

It is worthwhile to compare some of the details used in the present work to that used by Paukku *et al.*[?] to determine the $N_4$ potential. In their calculations, the "spectator" diatom was restricted to have only three different bond lengths: $R_e \pm 0.38 a_{\mathrm{o}}$, and the dissociating diatom had a bond length going from 1.5-11 $a_{\mathrm{o}}$. The dissociating diatom bond lengths are similar to what is used in the present work. For our $N_4$ potential, not described here, we used a 9 by 9 grid of bond lengths ranging from 1.8-3.1 $a_{\mathrm{o}}$ calculated using the CCSD(T) method, correlating 20 electrons. This was augmented by dissociation calculations using the icACPF method, correlating 12 electrons. The number of orientations Paukku *et al.* consider is only 8 for the $N_2$+$N_2$ geometries, which is much less than we use here. Unless one uses a very good model for the interpolating function, these will probably not be a sufficient number of angles. In our $N_4$ potential energy surface, we consider 9 orientations for $N_2$+$N_2$, but only consider 3 orientations for dissociating geometries. This, combined with a carefully chosen functional form, is expected to do a good job of representing the complete potential energy hyper-surface.
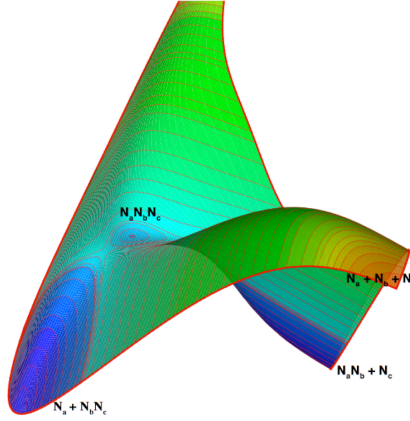
Figure 3: Analytical representation of the potential energy surface for $N_3$ (with the atoms labeled $N_a$, $N_b$ and $N_c$) in terms of $R(N_aN_b)$ and $R(N_bN_c)$ with the angle $< N_aN_bN_c$ fixed at $115^o$. Blue regions are lowest in energy and red are highest.

# 3 Collisional calculations to State-to-state Rate Coefficients

From statistical mechanics, the microscopic state-to-state rate coefficients are given by the following expression,[?]

$$k_{if}(T) = \frac{1}{3}(2k_BT)^{\frac{3}{2}}(\mu\pi)^{-\frac{1}{2}} \int_0^\infty \sigma_{if}(E_i)\, E_i\, \exp\left(-\frac{E_i}{k_BT}\right) dE_i, \qquad (17)$$

where i specifies the initial $(v, J)$ state, f the final $(v, J)$ state, $k_B$ is Boltzmann's constant, $T$ is the translational temperature, $\mu$ is the reduced mass for the reactants, equal to $2m_N/3$ for $N_2+N$ and $m_N$ for $N_2+N_2$, $m_N$ the mass of a nitrogen nucleus, and $\sigma_{if}$ is the integral cross section for transitions from i to f for initial state translational energy $E_i$. This expression applies to all bi-molecular collision processes, including elastic, inelastic, exchange and dissociative ones.

The integral cross section computed using quantum mechanics takes the form[?]

$$\sigma_{if} = \frac{\pi}{g_i k_i^2} \sum_{nl} \left|S_{in\,fl}(E) - \delta_{if}\delta_{nl}\right|^2, \qquad (18)$$

where $g_i$ is the degeneracy of state specified by i, $k_i$ is the initial state wave vector given by $k_i^2 = 2\mu E_i/\hbar^2$, $E_i = E - \epsilon(v,J)on_i$, with $\epsilon_i$ the energy of the $(v, J)$ state specified by i, and $S_{in\,fl}$ is the scattering matrix element giving the outgoing wave amplitude from entrance channel specified by $(v, J)$ state i and other quantum numbers n, to exit channel specified by $(v, J)$ state f and other quantum numbers l. The other quantum numbers would specify the "arrangement" of the nitrogen atoms, i.e. $N_a + N_bN_c$, $N_b + N_cN_a$, $N_c + N_aN_b$, or $N_a + N_b + N_c$, and the angular momentum quantum numbers related to the three-body system. The quantity $\delta_{ab}$ is a Kronecker delta, and is unity of $a = b$ and zero otherwise, and $|a|^2$ means $a^*a$, where $a^*$ is the complex conjugate of $a$. This is required because the scattering matrix is a complex symmetric unitary matrix.

14

For connection between quantum and classical mechanics, it is worth while elucidating what is meant by the angular momentum quantum numbers related to the three-body system. Several choices are possible, with the most simplistic being $m_j$, the projection of the diatom rotation on the space fixed z-axis (sfz) divided by $\hbar$, $\ell$, the orbital angular momentum of the atom divided by $\hbar$, and $m_\ell$, the projection of the atomic orbital angular momentum on the sfz divided by $\hbar$. This is called the uncoupled representation. Another useful choice is to form total angular momentum eigenfunctions, in which case the angular momentum quantum numbers are $\ell$, $J$, the total angular momentum quantum number, and $M$, the projection of the total angular momentum on the sfz divided by $\hbar$. A final choice is to use $J$, $M$, and $K$, where $K$ is the projection of the total angular momentum on the body fixed z axis divided by $\hbar$ (see Eq. 7 for the definition of the body fixed z axis). The scattering matrices in one representation can be analytically transformed into the other representations, and the computed cross section will be independent of the choice of the representation. The advantage of the total angular momentum representations in quantum calculations is that there is no dependence of the scattering matrix on $M$, and there is no coupling between different values of $J$.

The interpretation of the integral cross section is as follows: it has units area (think "target size"), and one can clearly see the factor $\frac{\pi}{k_i^2}$ is the formula for the area of the circle of radius $1/k_i$. The astute reader will notice that $1/k_i$ is essentially the De Broglie wave length defined earlier. The factor of $2\pi$ difference between $1/k_i$ and the De Broglie wave length arises from the convention of measuring frequency in terms of radians per unit time rather than cycles per unit time, and thus has no physical significance. If i$\neq$f, the rest of the expression for the integral cross section represents the probability of going from i to f, summed over all irrelevant qualities of f and averaged over all irrelevant qualities of i. For elastic scattering, i=f and we have to include the term $\delta_{nl}$, which is a purely quantum mechanical interference term.

Now let us consider not the transition from i to f but rather the transition from f to i. Assume that both i and f are for bound states of N$_2$. From statistical mechanics we know that

$$\frac{k_{if}}{k_{fi}} = \frac{Q_f}{Q_i} = \frac{g_f}{g_i} \exp\left(-\frac{\epsilon_f - \epsilon_i}{k_B T}\right), \tag{19}$$

where $Q_i$ is the partition function of level i, and similarly for f. Now let us derive this expression from Eqs. 17-18. The scattering matrix is symmetric, *i.e.* for a given total energy $E = E_i + \epsilon_i = E_f + \epsilon_f$, $S_{in\,fl} = S_{fl\,in}$, thus we see that

$$\sigma_{if}(E_i) = \sigma_{fi}(E_f)\frac{g_f}{g_i}\frac{k_f^2}{k_i^2} = \sigma_{fi}(E_f)\frac{g_f}{g_i}\frac{E_f}{E_i}. \tag{20}$$

Substituting this into Eq. 17 then yields Eq. 19. It should be noted that Eq. 19 is commonly referred to as detailed balance, whereas Eq. 20 is commonly referred to as microscopic reversibility, and these in turn follow from the symmetry of the scattering matrix, and that is due to time reversal symmetry.[?]

Before we move on to the classical treatment that we actually used in this work, it is valuable to motivate the use of that approximation by describing how one would go about carrying out a quantum mechanical calculation. The goal of quantum mechanics is to determine the wave function $\Psi^{in}$ that solves the Schrödinger equation:

$$i\hbar\frac{\partial}{\partial t}\Psi^{in} = H\Psi^{in}, \tag{21}$$

15

subject to the boundary conditions specified by in. In this equation, $i = \sqrt{-1}$, $t$ is time and the object $H$ is the Hamiltonian operator, and in the Born-Oppenheimer approximation, it is made up of the nuclear kinetic energy operator and the potential energy hyper-surface. We also require that $\Psi^{\text{in}}$ be regular, *i.e.* there are no regions of space where the average value of $\left|\Psi^{\text{in}}\right|^2 d\tau$ is not finite, where $d\tau$ is the volume element. Now $H$ has no time dependence, so we can write

$$\Psi^{\text{in}} = \exp(-iEt/\hbar)\psi^{\text{in}}, \tag{22}$$

with $\psi^{\text{in}}$ having no time dependence. The physical interpretation of $E$ is it is the total energy of the system. Then $\psi^{\text{in}}$ can be seen to satisfy

$$H\psi^{\text{in}} = E\psi^{\text{in}}. \tag{23}$$

Now we can solve this equation a wide variety of ways, but all start by making an expansion in terms of basis functions:

$$\psi^{\text{in}} = \sum_{\text{x}} \chi_{\text{x}} f_{\text{x}}^{\text{in}}(\rho_{\text{x}}, E) \tag{24}$$

where $\rho_{\text{x}}$ is the "scattering coordinate" for basis function x, $f_{\text{x}}^{\text{in}}$ is a unknown function, and $\chi_{\text{x}}$ is a known basis function that includes the dependence on all other coordinates. It is usual that included in the sum over x are all the terms fl occurring in Eq. 18, although for accurate results, the sum over x can not just consist of the fl.

Now we must find the $f_{\text{x}}^{\text{in}}$ subject to the boundary conditions specified by in. If in and fl refer to bound states of $N_2$, then $\rho_{\text{fl}} = r_{\text{l}}$, (See the discussion at the start of this chapter for the definition of $r_a$), so[?]

$$\lim_{r_{\text{l}} \to \infty} f_{\text{fl}}^{\text{in}}(r_{\text{l}}, E) = \frac{1}{r_{\text{l}}} k_{\text{f}}^{-\frac{1}{2}} \left[ \delta_{\text{if}} \delta_{\text{nl}} \exp(-ik_{\text{f}}r_{\text{l}}) - \exp(ik_{\text{f}}r_{\text{l}}) S_{\text{in fl}}(E) \right]. \tag{25}$$

The physical interpretation of this equation is there is an incoming wave (the $-ikr$ term) with unit amplitude along with a scattered wave (the $+ikr$ term) modulated by the complex coefficient $S_{\text{im fn}}$. As $E \to \infty$ or $\ell, J \to \infty$, there is no interaction, thus $S_{\text{in fl}} \to \delta_{\text{if}} \delta_{\text{nl}}$.

Now one way to solve for the $f_{\text{fl}}^{\text{in}}$ is to expand them in terms of known functions.[?] Then the unknowns become coefficients rather than functions. For sake of argument, say that we need $\mathcal{N}$ functions per $f_{\text{x}}^{\text{in}}$ to obtain accurate results. Then the determination of the unknowns for a single in requires the solution $\mathcal{N} \times N_{\text{x}}$ coupled linear equations, where $N_{\text{x}}$ is the number of basis functions x. Now using our $V^{NN}$, the $N_2$ molecule has about $10^4$ $(v, J)$ states, so the f part of fl in x is $\approx 10^4$. The l part of $N_{\text{x}}$ depends on what one uses for basis functions. In the total angular momentum representation, which is the basis that allows for maximum decoupling, the l functions fall into blocks of maximum size $J + 1$, where $J$ runs from 0 to 100 or more. Thus the number of coupled linear equations could easily exceed $10^6$ to $10^7$, depending on $\mathcal{N}$. This then, becomes a very, very formidable task.

Another possibility is not to solve for the $f_{\text{fl}}^{\text{in}}$, but rather use perturbation theory to solve directly for the scattering matrix. In perturbation theory, we partition the Hamiltonian operator $H$ into a part $H^0$ and the rest: $\Delta H = H - H^0$, and we assume that we can determine the Green's function for $H^0$. Then we can write[?]

$$S_{\text{in fl}} \approx S_{\text{in fl}}^0 + \Delta S_{\text{in fl}}^{\text{DWBA}}, \tag{26}$$

with $S_{\text{in fl}}^0$ the scattering matrix for the zero order problem and

$$\Delta S_{\text{in fl}}^{\text{DWBA}} = \frac{2\pi}{\hbar^2} \sum_{\text{xy}} \int f_{\text{x}}^{0\text{in}} \chi_{\text{x}}^* \Delta H \chi_{\text{y}} f_{\text{y}}^{0\text{fl}}, \tag{27}$$

where DWBA stands for distorted wave Born approximation, and $f_x^{0\text{in}}$ is the radial function for the zero order problem. The integral is over all space.

We can make $H^0$ such that the $f_x^{0\text{in}}$ is non-zero only for x=in, and similarly for fl, so this sort of calculation is feasible, however the reliability is another question. This route might be the only practical route for predicting low probability events, for in that case $f_x^{0in}$ and $f_y^{0fl}$ can be expected to provide a good description of the true case.

Another problem of a quantum treatment occurs when we have energy large enough to dissociate the $N_2$ molecule. Then the boundary conditions of Eq. 25 do not apply. In fact, the specific form of the boundary conditions still alludes researchers, and until recently, attempts to actually compute the dissociation cross section were limited to model problems. A very significant step forward occurred when McCurdy *et al.*[?] realized that by adding a complex absorbing potential to $H$ in Eq. 23, they could ensure that all flux heading to the double dissociation limit would be absorbed without effecting any of the other scattered flux. Then the computed scattering matrix would no longer satisfy the unitarity relation:

$$\sum_{\text{fl}} \left| S_{\text{in fl}}^{\text{ap}} \right|^2 \neq 1, \tag{28}$$

so that the dissociation integral cross section could be computed as

$$\sigma_{\text{id}} = \frac{\pi}{g_{\text{i}} k_{\text{i}}^2} \sum_{\text{n}} \left( 1 - \sum_{\text{fl}} \left| S_{\text{in fl}}^{\text{ap}} \right|^2 \right), \tag{29}$$

where the superscript ap on the scattering matrix means it is computed in the presence of an absorbing potential.

The microscopic dissociation rate coefficient is determined essentially by Eq. 17 using the dissociation cross section. To determine the microscopic recombination rate coefficient, we utilize the dissociation rate coefficient and statistical mechanics: *e.g.*

$$\text{k}_{\text{di}}/\text{k}_{\text{id}} = Q_{\text{i}}/Q_{\text{N}}^2, \tag{30}$$

where $Q_{\text{N}}$ is the atomic partition function and $Q_{\text{i}}$ is the partition function for $N_2$ level i.

Let us now turn to the classical simulation of the integral cross sections. The rough outline is we start with some initial conditions specified by i= $vj$ as well as some uninteresting initial conditions, then we integrate forward in time until the projectile is now flying away from the target and is in some new state f, and other uninteresting final conditions. We will do this many times for different values of the uninteresting initial conditions and average over them. An important difference right off the bat between the classical and quantum calculations is that in the classical calculations, a given set of initial conditions produces only one final condition, where as in quantum calculations, a single initial quantum state gives rise to all possible final states. This is a very important feature that will motivate how we do the averaging. This is discuss further below.

Now to implement this is practice, we need to know how to specify the initial condition i and analyze for the final condition f. This requires that we know how the quantum numbers $(v, J)$ relate to the motion of the $N_2$ molecule. The way to do this has its birth in the Einstein[?]-Brillouin[?]-Keller[?] (EBK) quantization condition, and formally it requires a transformation to "good action-angle variables". Let us explain this. The classical description of particles is most conveniently given by the solution of Hamilton's equations:[?]

$$\dot{x} = \frac{\partial \text{H}}{\partial p} \tag{31}$$

17

$$\dot{p} = -\frac{\partial \text{H}}{\partial x}, \tag{32}$$

where $x$ is some coordinate, dot means time derivative, $p$ is the momentum conjugate to $x$, and H is the sum of the classical kinetic energy (T) and the potential energy ($V$). If $x$ is a cartesian coordinate, then $p = m\dot{x}$ with $m$ the mass for $x$, and H= $\frac{p^2}{2m} + V(x)$. Then Hamilton's equations reduce to $-\frac{\partial V}{\partial x} = m\ddot{x}$, or Newton's second law, force is mass times acceleration. The real beauty of Hamilton's equations is not revealed until complex coordinate and momentum transformations are made. In particular, suppose by some hook or crook one could transform to a new variable $\theta$ and conjugate momentum $I$ such that H= $f(I)$, where $f$ is some function. Then Hamilton's equations tell us that

$$\dot{\theta} = \frac{\partial f(I)}{\partial I} = f'(I) \tag{33}$$

and

$$\dot{I} = -\frac{\partial f(I)}{\partial \theta} = 0. \tag{34}$$

We can integrate these equations by inspection: $I(t) = I(t_o)$ and $\theta(t) = \theta(t_o) + f'(I)(t - t_o)$, where $t_o$ is the initial time. In this situation it is said that we have found good action-angle variables, and the momentum $I$ is the action variable and the coordinate $\theta$ is the angle variable. Then the EBK quantization condition is that the action $I$ can only take on the values $I = \hbar(n + \frac{1}{2})$, where $n$ is a non-negative integer.

Let us illustrate this by an example. Suppose $V = \frac{1}{2}m\omega^2 x^2$, *i.e.* the potential for a harmonic oscillator. As time goes forward, we know that $x$ oscillates back and forth between the turning points, and that $p$ also oscillates back and forth with $p$ zero at the turning points and maximum when $x = 0$. Thus it does not seem unreasonable to try

$$x(t) = a \sin bt. \tag{35}$$

Then we see

$$\dot{x} = ab \cos bt = \frac{p}{m}. \tag{36}$$

thus

$$p = mab \cos bt \tag{37}$$

and

$$\dot{p} = -mab^2 \sin bt = -m\omega^2 x = -m\omega^2 a \sin bt. \tag{38}$$

We then see that $b^2 = \omega^2$ and H= $\frac{m}{2}a^2\omega^2$ is independent of time. This then suggests that if we take $\theta = bt$, we can write H without $\theta$ and have found our good action-angle variables. To define the action variable $I$, we note that $\dot{\theta} = f'(I) = \omega$, which then implies that H= $I\omega$, or $I = \frac{m}{2}a^2\omega$. Then the EBK quantization condition for the energy becomes H=$\hbar\omega(n + \frac{1}{2})$, which we recognize as being identical to the quantum mechanical result.

So in analogy to the quantum mechanical situation where we have the interesting quantum numbers $(v, J)$ and the uninteresting ones specified by n, in the classical treatment the interesting labels are the action variables for vibration and rotation, and the uninteresting ones include the angle variables for vibration and rotation.

Now the harmonic oscillator problem is very simple, and we must deal with real world examples that are not nearly so simple. To do this properly, one has to deal with the diatomic Hamiltonian

$$\text{H} = \frac{p_R^2}{2m} + \frac{p_\chi^2}{2mR^2} + V^{NN}(R) \tag{39}$$

18

where $p_R$ is the momentum conjugate to the diatomic bond length $R$ and $p_\chi$ is the momentum conjugate to the rotation angle $\chi$. We take the diatom to lie in the xz plane and $\chi$ to be the angle rotating the z axis to the diatom bond axis. Because $V^{NN}$ is a complicated function and because H couples $R$ and $\chi$, the determination of good action-angle variables must be done numerically, and Eaker[?] has shown how to do this. It involves choosing an set of initial conditions for $R$, $p_R$, $\chi$, and $p_\chi$, numerically integrating the equations of motion forward in time for a suitability long period of time, then carrying out a Fourier transformation to express the coordinates and momenta in the frequency domain rather than the time domain. The Fourier coefficients are then analyzed to find the peak heights and peak spacing. From these one can determine the actions and express the $R$, $p_R$, $\chi$, and $p_\chi$ as a function of the angle variables. This is a rather complicated process, for example, the length of time one integrates the trajectories prior to applying the Fourier transformation determines the resolution in the frequency domain spectrum, thus variable amounts of time will be required depending on the initial conditions. Thus we use a simplified approach.

In our approach, we take advantage of the fact that for a one dimensional problem, the integral $\oint p\,dq$ is independent of the choice of coordinates, where $\oint$ means the integral over one period of oscillation. This integral is easily evaluated in action-angle variables: it equals $2\pi I$. Then if we take $p_\chi = \hbar(j + \frac{1}{2})$, to solve the vibrational problem we need to find the energy $\epsilon_{vj}$ that satisfies the EBK quantization condition, $i.e.$

$$\oint p\,dq = 2\int_{R-}^{R+} \sqrt{2m\left[\epsilon_{vj} - V^{NN} - \frac{\hbar^2(j+\frac{1}{2})^2}{2mR^2}\right]}\,dR = h\left(v + \frac{1}{2}\right), \tag{40}$$

where $R\pm$ are the classical turning points and the quantity under the radical is $p_R$ found by inverting Eq. 39. We can evaluate the integral accurately using the appropriate Gaussian quadrature, and then this is just a non-linear root finding problem.[?]

This tells us $\epsilon_{vj}$ for the initial state, but not $R$, $\chi$, $\dot{R}$, and $\dot{\chi}$ that are required to actually set up the initial conditions for the molecule. To do this, we must specify the angle variables, but we do not know the relation between the angle variables and the physical variables. But we do know that the angle variable and time are linearly related, so if $\tau_{vj}$ is the period of oscillation for state $(v, J)$, then if $\theta_0$ is the angle variable we want to start from, we can just as well set $R = R+$ and $p_R = 0$, and the integrate the equations of motion for $R$ and $p_R$ (Hamiltonian's equations generated from Eq. 39) forward in time the amount $\tau_{vj}\theta_0/2\pi$. Then $R$ and $p_R$ at time $\tau_{vj}\theta_0/2\pi$ are the quantities we require. This is easy to do once we have $\tau_{vj}$, but fortunately $\tau_{vj}$ is found easily by

$$\oint (\dot{R})^{-1}dR = \tau \tag{41}$$

where $\dot{R} = p_R/2m$ from Eqs. 31 and 39.

We are left with the specification of $\chi$. This is a much harder nut to crack, and to do things properly, one could follow a procedure such as that described by Eaker.[?] The problem is although $\chi$ runs from 0 to $2\pi$, it does not do so linearly in time, for there is the $1/R^2$ factor in $\dot{\chi}$, and $R$ also depends on time. Nonetheless we will assume that reasonable results can be had by sampling $\chi$ uniformly. As an assessment of the error caused by this, we show in Fig. 4 $\chi$ as a function of time for selected values of $(v, J)$. In this figure, the arrows mark the vibrational period, and the curves repeat themselves for each vibrational period. The rotational periods are several times the vibrational periods, so an accurate calculation would first select the vibrational angle variable, which would then tell one where to start on the curve, then one would select the angle variable,

and that would tell you how far to move along the curve to get the starting value of $\chi$. In any case, the departure from linearity does not seem to be large enough to cause concern.
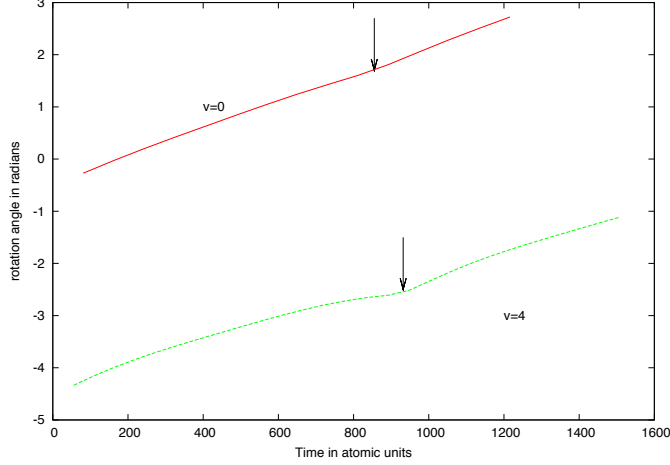


Figure 4: Rotation angle as a function of time for $j = 100$.

Now consider the analysis of the final condition of a trajectory. From the final diatom positions and velocities, we can compute the angular momentum of the diatom: $p_\chi$. Then we can compute the angular momentum quantum number as $j = \frac{p_\chi}{\hbar} - \frac{1}{2}$. Next we compute the vibrational quantum number $v$ by evaluating Eq. 40 with the final internal energy of the diatom. Now we have $v$ and $j$, but in general, they will not be integers. The simplest way to proceed is to now make them integers by replacing them with the closest non-zero integer. This is basically what we do. What we do that is not that, is if the collision is non-reactive, then we have a further restriction that $\Delta j$ must not be odd, since $N_2$ is a homo-nuclear diatom. In this case, we find the closest integer to $\frac{j-\delta}{2}$, where $\delta$ is the remainder when the initial $j$ is divided by 2, and then set $j$ to twice this integer plus $\delta$.

It is immediately clear from the determination of the final conditions that there is an inherent asymmetry between computing i→f and f→i: the initial $(v, J)$ are integral whereas the final $(v, J)$ are not. Thus, when computing cross sections from classical mechanics, the relation of Eq. 20 will not be satisfied, and to ensure proper equilibrium, we must force Eq. 20 to be satisfied. We believe that one of $\sigma_{fi}$ or $\sigma_{if}$ will be computed more accurately than the other, and so we will discard the less accurate one and instead compute it from the more accurate one and Eq. 20. We assume that the more accurate one will be the cross section computed in the exothermic direction, *i.e.* the direction where the final state has lower energy than the initial state.

Now it turns out with classical mechanics we can compute the square of the S matrix element, directly compute the cross section without computing the S matrix elements, or directly compute the microscopic rate coefficient without computing the cross section. To understand this, let us first consider the calculation of the square of the S matrix in the uncoupled representation.

In the uncoupled representation, i= $vj$ and n=$m_j, \ell, m_\ell$. We have described how we can get $R$, $\dot{R}$, $\chi$, $\dot{\chi}$ specified by i= $vj$ and $\theta_v$ and $\theta_\chi$. To orient the diatom angular momentum vector in space, we need to make the z component $m_j$, but are still free to choose the x and y components: we do this by specifying the variable $\theta_j$. We will place the center of mass of the diatom at the origin. Similarly, we need to choose initial conditions for the atom such that the orbital angular momentum has magnitude $\ell\hbar$ and z axis component $m_\ell\hbar$. Again, the x and y components are unspecified, so we fix them by specifying the variable $\theta_\ell$. We will place the atom a distance $d$ from the origin. Now we can run the trajectory until an atom-atom distance is greater than $d_f$, with $d_f > d$. At this point we can analyze the final state of the diatom.

That is one trajectory. To get the square of the scattering matrix element, the probability of going from in to fl, we need to average over $\theta_v$, $\theta_\chi$, $\theta_j$, and $\theta_\ell$. Since these are continuous variables, the average takes the form of a four-dimensional integral, with the integrand the measure of whether or not those $\theta$s led from in to fl: this measure is either zero or one. The important thing to note is the integrand is not at all smooth, and no derivatives exist. Thus classic quadrature schemes will give very poor results if they are used to evaluate these integrals. Really the only way to evaluate these integrals is to use the Monte-Carlo method. Here we randomly choose the values of $\theta_v$, $\theta_\chi$, $\theta_j$, and $\theta_\ell$ $N$ times, and the value of the integral apart from prefactors is $N_{\text{in fl}}/N$, where $N_{\text{in fl}}$ is the number of trajectories that started with initial condition in and ended with final condition fl. An important by product of the Monte-Carlo method is the estimate of the error in the internal. It is proportional to $1/\sqrt{N}$. This error estimate is a two edged sword: on one hand the convergence is rather slow: to halve the error, one would have to run four times as many trajectories. But on the other hand, the error estimate is independent of the number of dimensions in the integral. This last observation has huge consequences: Rather than individually computing the hundreds or thousands of terms entering into the cross sections, if we change the sums over n and l into integrals, with the same number of trajectories we can compute the cross sections with an accuracy 10-30 times better.

Similarly, if the ultimate goal is the microscopic rate coefficient, rather than computing the cross section as a function of energy, and then evaluating Eq. 17, we can throw the $E_i$ integration into the Monte-Carlo procedure as well and get better results with fewer trajectories.

Now consider how we change the sum over $\ell$ and $m_\ell$ into integrals. Now $m_\ell$ is the projection of $\ell$ onto the space-fixed axis system. But we do not have to carry out the trajectories in the space-fixed axis system, rather we will carry out the trajectories in the body-fixed axis system. Recall that in the body-fixed axis system, we require the center of mass of the system to be stationary at the origin. However, it is useful to set up the initial conditions with the atom in the xy plane and the diatom center of mass stationary at the origin. Then the initial coordinates and momentum of the atom are $b, d, 0$ and $p_i, 0, 0$, where $p_i = -\sqrt{2\mu E_i}$. The quantity $b$ is called the impact parameter, and is the distance of closest approach of the atom to the center of mass of the diatom if there was no interaction. Then the initial orbital angular momentum is $0, 0, -p_i b$. So the first observation we make is that our body-fixed axis system is chosen in such a way to be independent of $m_\ell$. Thus we can analytically perform the sum over $m_\ell$, and the result is $2\ell + 1$. Thus we need to evaluate the sum $\sum_\ell (2\ell + 1)P(\ell)$. To do this, it is convenient to change variables from $\ell$ to $b$: they are related by $\ell\hbar = p_i b$. Now let us consider for a moment the likely sizes of $\ell$. At the start of this section we mentioned that at T=10,000K, a nitrogen atom would have $p \approx 40$ a.u. Then if we assume that $\tilde{P}(b) = P(p_i b/\hbar)$ is independent of $b$ until the impact parameter reaches some maximum value, say $b_{\max}$, and taking $b_{\max} = R_e/2 \approx 1$ a.u., we see that $\ell$ will run from 0 to 40, and $\sum_\ell (2\ell + 1)P(\ell) = 41^2 P(0) = 1681 P(0)$. If instead we replaced $2\ell + 1$ with $2\ell$, the sum would

be $1640P(0)$, for an error of only 2.4%. This is an acceptable error, so henceforth we use $2\ell$ instead of $2\ell + 1$. Now the way to turn the sum over $\ell$ into an integral is the Euler-MacLaurin summation formula, *i.e.*

$$\sum_\ell 2\ell P(\ell) \approx \int_0^{\ell_{\max}} 2\ell P(\ell) d\ell \tag{42}$$

where we have used the fact that the lower limit and upper limits give no contribution to the integral. Then, changing variables from $\ell$ to $b$ gives us

$$\frac{2p_i^2}{\hbar^2} \int_0^{b_{\max}} \tilde{P}(b) b \, db. \tag{43}$$

If $\tilde{P}(b)$ is independent of $b$, then the integral can be done analytically, and we obtain $\tilde{P}(0)\frac{p^2 b_{\max}^2}{\hbar^2}$, so that the cross section becomes

$$\sigma_{if} = \tilde{P}(0)\frac{\pi b_{\max}^2}{g_i}, \tag{44}$$

*i.e.* the area of the circle of radius $b_{\max}$ times the probably of going from i to f divided by the degeneracy factor.

Now in actuality, $\tilde{P}(b)$ is not independent of $b$, and we actually have to carry out the integral. Now to do the integral by Monte-Carlo methods, we need to change variables to achieve a constant volume element and integration range 0 to 1, and this is done by the substitution $\theta = (\frac{b}{b_{\max}})^2$, so that

$$\int_0^{b_{\max}} f(b) b \, db = \frac{2}{b_{\max}^2} \int_0^1 f(\sqrt{\theta}\, b_{\max}) d\theta. \tag{45}$$

The problem with using this form for the integral is uniformly sampling on $\theta$ will tend to more likely sample $b$ near $b_{\max}$ than near $b = 0$, and since $b_{\max}$ is chosen so that $\tilde{P}(b_{\max}) = 0$, this means the Monte-Carlo method will give even slower convergence. Thus we use a stratified sampling technique. [?] Here we choose a sequence of $b_{\max}$ values so we can concentrate $b$ to small values for low probability events as well as allow for larger values for high probability events. The sequence we use is $b_{\max}=0.25$, 0.5, 1, 3, 5, and 8 $a_o$.

Now let us consider elastic scattering for a moment: the case where f=i. In quantum mechanics, here the $-\delta_{if}\delta_{nl}$ term comes into play and the cross section is finite. In classical mechanics, in the limit $b \to \infty$ the probability of going from i to f=i becomes unity. Thus in classical mechanics, the elastic cross section is infinite and it is not possible to compute the elastic cross section from classical calculations. Fortunately for our purposes, the elastic cross section plays no role in our kinetics calculations.

For direct simulation monte carlo (DSMC) flow calculations, it would be nice to compute transport properties during the simulations. To do this, one requires not the integral elastic cross section, which can not be computed from classical mechanics, but rather the integral of the elastic differential cross section $d\sigma/d\Omega$ times the weighting function $1 - \cos^l \theta$, with $l = 1, 2$ or 3. In quantum mechanics, the $\delta_{if}\delta_{nl}$ term serves two purposes: firstly it ensures the finiteness of the integral cross section, and secondly it causes the differential cross section to be a highly oscillatory. In classical mechanics, the integral cross section diverges because the differential cross section at zero $\theta$ becomes infinite. However the factor $1 - \cos^l \theta$ should remove this singularity so that finite integrals can be computed. Also, this oscillatory behavior of the quantum results will not be present in classical simulations, but since the important collision integrals include factors that are not strong

functions of angle for $\theta$ significant different from zero, the classical calculations should be able to give reasonable results.
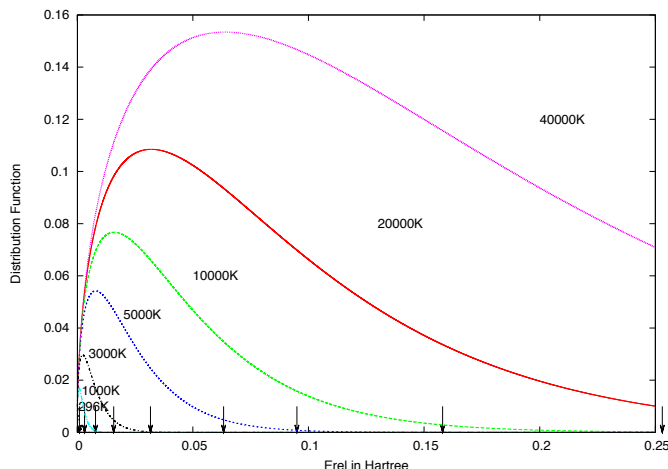


Figure 5: Unnormalized Relative Translational Energy distributions

Now let us discuss the selection of the initial relative translational energies. In Fig. 5 and 6 we show the Boltzmann distribution for several temperatures. In this figure, the maximum probability is normalized to unity. We see that at low temperature, say 300K, the energy distribution is very sharply peaked. In contrast, at high temperature, say 20,000K, the energy distribution is very, very broad. Now if one is considering a range of temperatures, as is the case in the present work, one has two choices to select the relative translational energies. In the first case, we compute the cross sections at specific representative energies, and in the figure we indicate with arrows what those energies might be. A second choice is to assume a translational temperature and sample the energy from the Boltzmann distribution at that temperature. We then will bin the energies, and compute a cross section representative for this bin. In this later choice, energies that are unlikely will not be sampled often, and thus efficiencies are gained. This choice will only be usable when the Boltzmann distribution is not that different for all translational temperatures of interest. In our work, we sampled the translational energy from a 60,000K Boltzmann distribution. Thus we can reliable predict state-to-state rate coefficients only down to about 5000K. This should not be a limitation for the type of simulations we are currently interested in doing.

We have thus described the calculation of cross sections and rate coefficients for transitions between bound states. Now we need to extend the discussion to include quasi-bound states and dissociated states.

First consider quasi-bound states. These are states for which one can find good action-angle variables in classical mechanics, but in quantum mechanics these states can decay to atoms via tunneling through the centrifugal barrier (the $p_\chi^2/2mR^2$ term in Eq. 39). These states are called different things in different fields of study: in spectroscopy they are called pre-dissociated states,
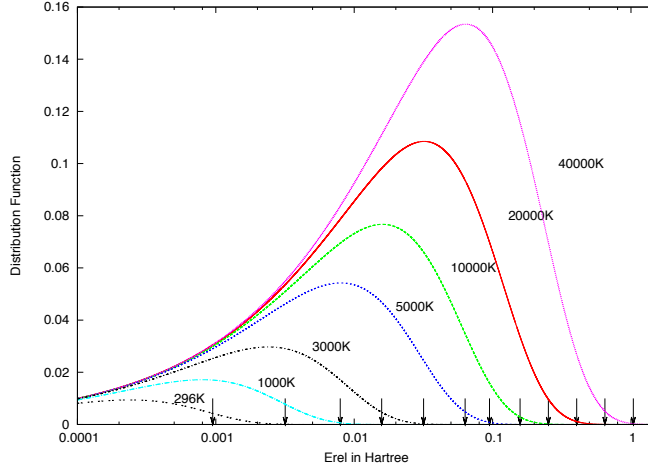
23

Figure 6: Unnormalized Relative Translational Energy Distributions

and in quantum scattering theory they are called resonant states.[?] The properties of these states has been studied intensely via formal scattering theory, and the salient results is they are very much like true bound states, except rather than having quantized energies on the real energy axis, they have quantized energies in the complex energy plane: call this energy $E_{vj} - i\Gamma_{vj}/2$ with $E_{vj}$ and $\Gamma_{vj}$ real. Of course, the physical energy axis is the real energy axis, thus the imaginary part of the quantized energy, $\Gamma_{vj}$ is observed only indirectly. Commonly $\Gamma_{vj}$ is called the width of resonance $(v, J)$, for a feature in the optical spectra involving this state looks like a Lorentzian with full width at half max equal to $\Gamma_{vj}$ if the resonance is isolated. Furthermore, the uni-molecular decay rate of this state given by $\hbar/\Gamma_{vj}$. Thus the computation of $\Gamma_{vj}$ will be important for our simulations.

In classical mechanics, there is no way to compute the width $\Gamma_{\alpha}$, for in classical mechanics this state $\alpha$ is actually bound. What we do is use what is called a semi-classical procedure. Rather than start with classical mechanics and quantizing the actions, as described above, one can also start with quantum mechanics and assume a particular form for the wave function and expand in powers of $\hbar$. The simplest form, the primitive WKB method, gives exactly the same result as above for the vibrational energy levels. Then the next level, called the uniform semi-classical method, yields a correction to Eq. 40 as well as a nonzero result for $\Gamma_{vj}$. In our work, we neglect the correction to Eq. 40 for $\epsilon_{vj}$, but we use the uniform semi-classical result for the width:

$$\tau_{vj}\Gamma_{vj} = \hbar\exp\left\{-\int_{R+}^{Ro}\sqrt{2m\left[V^{NN} + \frac{\hbar^2(j+\frac{1}{2})^2}{2mR^2} - \epsilon_{vj}\right]}dR/\hbar\right\}, \tag{46}$$

where $Ro$ is smallest distance greater than $R+$ for which the radial in the integrand is zero.

So by these means we can easily compute $\epsilon_{vj}$, $\tau_{vj}$, and $\Gamma_{vj}$. Now for initial conditions, we follow the procedure described above for bound states, except we now do not just use the initial energy

24

$\epsilon_{vj}$, but rather sample from a gaussian distribution with center $\epsilon_{vj}$ and width $\Gamma_{vj}$.

## 3.1    Results of the Quasi-classical Trajectory Calculations

In the previous section discussed how collision cross sections $\sigma_{if}$ and state-to-state rate coefficients $k_{if}(T)$ can be simulated using the classical equations of motion with all the necessary parameters selected by Monte Carlo sampling schemes. Now we show how thermal rate coefficients for $N_2$ + N and $N_2$ + $N_2$ collisions are obtained from the state-to-state rate coefficients. The thermal rate coefficient is defined through the chemical kinetics rate equation for the process $N_2$ + N $\rightarrow$ products:

$$\frac{dn_{N_2}}{dt} = k(T)n_{N_2}n_N, \tag{47}$$

where $n_X$ is the gas density of species $X$ in molecules/cm$^3$ and t is time in seconds. Thus the rate coefficient has units of cm$^3$ molecule$^{-1}$ second$^{-1}$. Sometimes rate coefficients are expressed in molar units by multiplying k by Avogadro's number. The thermal rate coefficient is obtained as the summation of the state-to-star cross sections multiplied by the Boltzmann weighting of each ro-vibrational level.

First we need to enumerate the ro-vibrational levels that are obtained by using the the modified Leroy potential for the $N_2$ molecule with the addition of a centrifugal term due to rotation and solving the Schrödinger equation for the nuclear motion. the potential ($V_J$) for a rotating and vibrating diatomic molecule is

$$V_J(R) = V_{J=0} + J(J+1)\frac{\hbar^2}{2\mu R^2}. \tag{48}$$

$V_J = 0$ is the rotation less potential, in this case the modified Leroy[?] expression, $J$ is the rotation quantum number, $\mu$ is the reduced mass of the diatomic molecule, N/2 for $N_2$, and $R$ is the distance between the atoms in the molecule. We use the semi-classical WKB approximation to obtain the ro-vibrational energy levels and vibrational wave functions. The addition of the centrifugal term produces an energy barrier in the diatomic potential for $J \gg 0$. Energy levels that lie above the dissociation energy (D$-e$ and below this barrier have finite lifetimes and are labelled as quasi bound. For $N_2$, most of these quasi bound levels have lifetimes considerably longer than the time between collisions and should be considered in the calculation of state-to-state rate coefficients. The rotating potential for $N_2$, based on the Leroy expression is shown in Fig. 3 for various values of $J$.

For the Leroy $N_2$ potential with $J = 0$ there are 61 vibrational levels ($v$ = 0,1,60) and for $J \neq$ 0, there is at least one bound vibrational level for values of $J$ up to 279[?, ?]. Figure 7 shows the potentials for 8 values of $J$ including $J = 0$ and 279. For larger values of $J$ the potential does not exhibit a minimum for finite R. In all there are 9390 bound and quasi bound ro-vibrational levels of $N_2$ as expressed by the modified LeRoy potential. Of these 7421 are bound and 1969 are quasi-bound. Most of the levels lie within 20 kcal/mol of the $N_2$ dissociation energy, which is 224.93 kcal/mol (D$_0$). The energy of the highest ro-vibrational level ($v = 0, J = 279$) is 344.09 kcal/mol. For increasing $J$ the effective dissociation energy (the difference between the centrifugal barrier and the energy of the (0,$J$)level) drops from D$_0$ to near zero. For $J = 136$ it is 140.61 kcal/mol and for $J = 230$ it is 36.27. In addition, the vibrational spacing, E(1,$J$) - E(0,$J$), is 2329 cm$^{-1}$ for $J = 0$ and 1327.8 cm$^{-1}$ for $J = 230$. Similarly, the rotational spacing (defined as E(0,$J + 1$) - E(0,$J$))
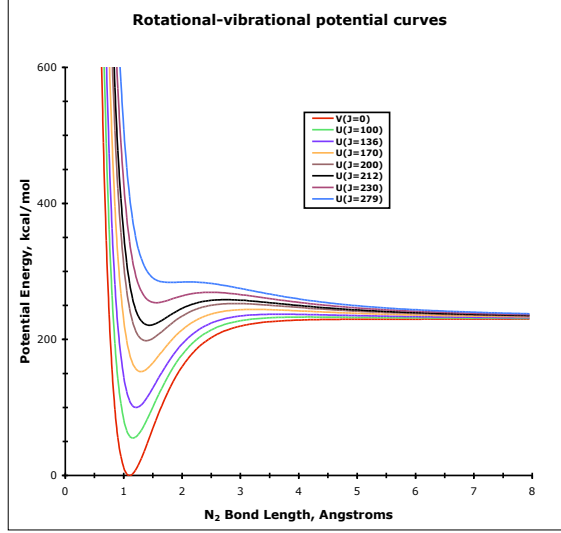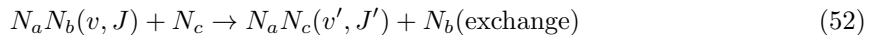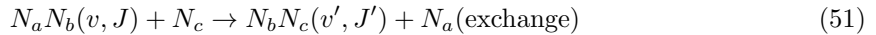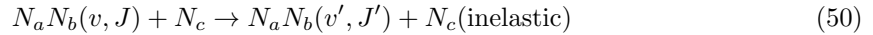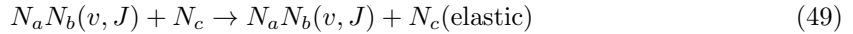
Figure 7: Potential energy curves for $N_2$. $V^{\mathrm{NN}}$ has units of kcal/mol and the bond length R is in Angstroms.

is 4.0 cm$^{-1}$ for $J = 0$ and 641.2 cm$^{-1}$ for $J = 230$. The dependence of these values on $J$ is a manifestation of the strong coupling between rotation and vibration[?].

We have computed state-to-state rate coefficients for $N_2$ + N pairs for each of these levels using the Quasi-Classical Trajectory method. The translation energy was sampled from a 20,000 K thermal distribution using a discrete set of 64 energies between 6.5 and 1160 kcal/mol with a thermal weighting factor of $0.5E_{rel}\exp(-E_{rel}/k_{\mathrm{B}}T)$. A batch of 6000 trajectories was run for each $N_2$ $(v, J)$ level. The individual trajectories in each set can be re-weighted for a different temperature so that cross sections and rate coefficients can be computed at other temperatures as well. With the range of $E_{rel}$ values used in these calculations, we can compute energy transfer rate coefficients for a range of temperatures from $\approx$7500 to 40,000 K. With the random sampling scheme used for initial conditions of each trajectory, the statistical error associated with each computed cross section is inversely proportional to the square root of the sample size. In our work the most of the individual state-to-state cross section values have statistical errors of 20% or less. Other sources of error are difficult to quantify; these include the accuracy of the quantum chemical potential and the fidelity of the analytic fit of the PES. The final states of these trajectories depend on whether the collision is elastic (no translation to internal energy transfer), inelastic or an exchange reaction (with translation to internal energy transfer), or dissociating:

$$N_aN_b(v, J) + N_c \rightarrow N_aN_b(v, J) + N_c(\text{elastic}) \tag{49}$$

$$N_aN_b(v, J) + N_c \rightarrow N_aN_b(v', J') + N_c(\text{inelastic}) \tag{50}$$

$$N_aN_b(v, J) + N_c \rightarrow N_bN_c(v', J') + N_a(\text{exchange}) \tag{51}$$

$$N_aN_b(v, J) + N_c \rightarrow N_aN_c(v', J') + N_b(\text{exchange}) \tag{52}$$

$$N_a N_b(v, J) + N_c \rightarrow N_a + N_b + N_c \text{(dissociative).} \tag{53}$$

All of these outcomes are possible. However, our sampling of initial conditions for the classical trajectories is not designed to yield an accurate determination of the elastic scattering cross section and corresponding rate coefficient. Figure 8 displays all the state-to-state inelastic (above the diagonal) and exchange rate coefficients (below the diagonal) for T = 10,000 K. Both kinds of processes have the largest rate coefficients clustered near the diagonal, which means that smaller amounts of energy transfer are more probable. However, the distribution of exchange rate coefficients shows greater width, indicative of larger amounts of energy transfer. The yellow region on the plot shows rate coefficients that are $\approx 10^3$ times smaller than those near the diagonal. Thus, the red region of the plot represents the important energy transfer processes at 10,000 K. Note that these rate coefficients extend through the energy range of the quasi-bound ro-vibrational energy levels (do-vibrational greater than 9.75 eV).
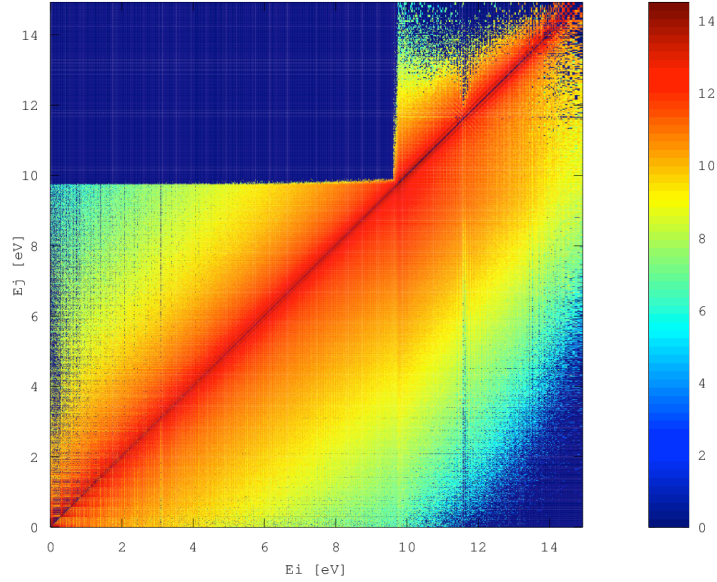


Figure 8: Molar rate coefficients in cm$^3$ mole$^{-1}$ second$^{-1}$ for inelastic and exchange processes at T = 10,000 K. Log($k_{ij}$) is plotted for ro-vibrational energies $E_i$ and $E_j$ with $i$ and $j$ referring to initial and final N$_2$ $(v, J)$, respectively. The diagonal starting at the origin represents the elastic channel. Inelastic rate coefficients are plotted above the diagonal and exchange rate coefficients are potted below. The color key is given on the right.

A similar illustration for the dissociation rate coefficients for N$_2(v, J)$ is shown in Fig. 9. The largest dissociation rate coefficients are for $(v, J)$ with rotation quantum number near the maximum value for each vibration quantum number. All the levels with $J$ greater than $\approx 215$ are in the quasi bound region. The light blue through red region of the plot represent rate coefficients that are important contributors to overall dissociation reaction.

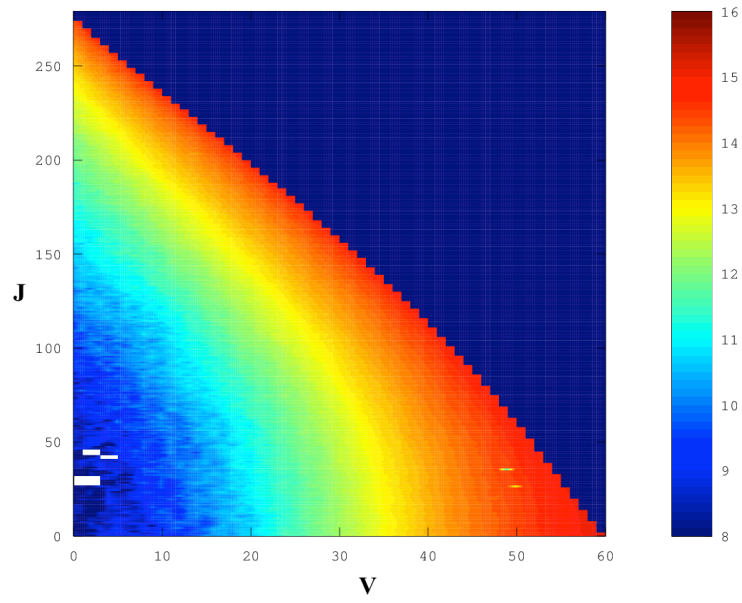The full set of rate coefficients shown in Fig.s are used to determine phenomenological rate

27

Figure 9: Molar rate coefficients in $cm^3$ per mole per second for dissociation processes at T = 10,000 K. $Log(k_{ij})$ is plotted for each value of vibration and rotation quantum numbers. The jagged red-orange line represents the highest value of $J$ for each $v$. The color key is given on the right.

coefficient that are discussed in the next section. It is of interest, however, to see how the thermal dissociation rate coefficient obtained from the state-specific dissociation rate coefficients agrees with the published results of shock tube experiments of the dissociation of $N_2$, in $N_2$/Ar mixtures, during the 1960's and 70's. These are the work of Cary[?] for the temperature range 6000-10,000 K, Byron[?] for 6000-9000 K, Appleton *et al.*[?] for the 8000-15,000 K and Hanson and Baganoff[?] for 6000-12,000 K. In these papers Arrhenius fits to the dissociation rate coefficient are given for $N_2 + N_2$, $N_2 + N$ and $N_2 + $ Ar. These rate coefficients are $\approx$5 times smaller than the results of the other shock tube experiments.In general, it is found that the $N_2 + N$ reaction is 4-8 times faster than $N_2 + N_2$. Park[?, ?] chose to use Appleton's values[?] for the $N_2 + N$ and $N_2 + N_2$ dissociation rate coefficients for his 2-T model, because the experimental data extend to higher temperatures. However he increased the pre-exponential factor to obtain better agreement of his 2-T model with experimental data. Our thermal rate coefficient for $N_2 + N$ is compared with the result of Appleton in Fig. 10.The agreement between the QCT and Appleton results is quite good, but the two determinations have different slopes. This is due to the QCT rate coefficient being well described by a two-parameter Arrhenius expression while the Appleton result is fit to a 3-parameter one. It can also be seen, by comparing the green (bound and quasi bound initial levels) and red (bound levels only) curves that dissociation from the quasi bound levels of $N_2$ makes an important contribution to the thermal dissociation rate coefficient at these temperatures. We have also obtained thermal rate coefficients for the $N_2 + N_2$ dissociation reaction using the QCT method and the $N_4$ PES. This rate coefficient is compared with experimental determinations in Fig. 11. The QCT rate coefficients (red asterisks) are in very good agreement with Appleton's and Byron's[?] measurements. On the other had, Hanson's determination[?] has a markedly different variation with temperature. The Park and Appleton rate coefficients also exhibit more Arrhenius curvature than does the QCT result. In general, one can conclude that the QCT method using the PES's described in this chapter yield thermal rate coefficients that are within a factor of two of the best shock tube determinations for $N_2$ dissociation. It should be noted that similar QCT calculations for $N_3$ have been carried out by Esposito, Colonna and Capitelli[?] using an empirical PES. They did not obtain results for all initial $v, J$ levels of $N_2$, but were able to draw some inferences about the effect of rotation on $N_2$ dissociation and collisional energy transfer.

# 4  Phenomenological rate coefficients from a detailed Master Equation model

It is not practical to use the full set of state-to-state rate coefficients in flow-field calculations. However, we can use these rate coefficients to develop a new ro-vibrational collisional model free of any assumptions about the temperature distribution of the ro-vibrational energy levels. We have carried out this analysis for a zero-dimensional chemical reactor and a 1-D shock wave. The zero dimensional analysis aims at unraveling the main features of state-to-state kinetics in a controlled environment free of the complications introduced by the flow chemistry coupling.[?] The system examined is a mixture of molecular nitrogen and a small amount of atomic nitrogen. This mixture, initially at room temperature, is heated by several thousands of degrees Kelvin, driving the system toward a strong non-equilibrium condition. The evolution of the population densities of each individual rovibrational level is explicitly determined via the numerical solution of the master equation for temperatures ranging from 5,000 to 50,000 [K]. The shock wave analysis aims at investigating the coupling of the detailed kinetics with the flow. The master equation is coupled
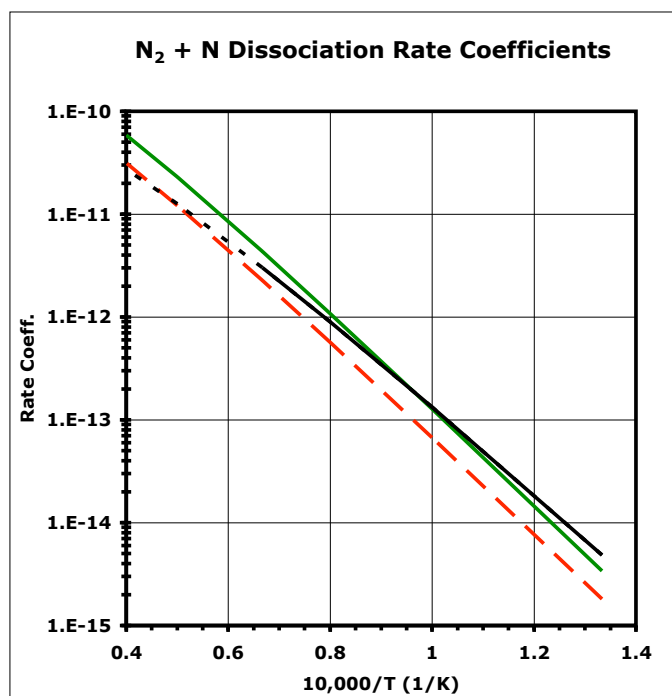
Figure 10: Thermal rate coefficients for $N_2$ dissociation due to collision with N atoms. The green line is the QCT result using all bound and quasi-bound initial energy levels for $N_2$. The red dashed line is the QCT result using only the bound $N_2$ energy levels. The black line is the rate coefficient determined by Appleton (Ref. [?]) as a fit to his shock tube data. The solid black portion represents the upper end of the measured temperature range and the dotted black portion is an extrapolation of Appletons expression to higher temperatures
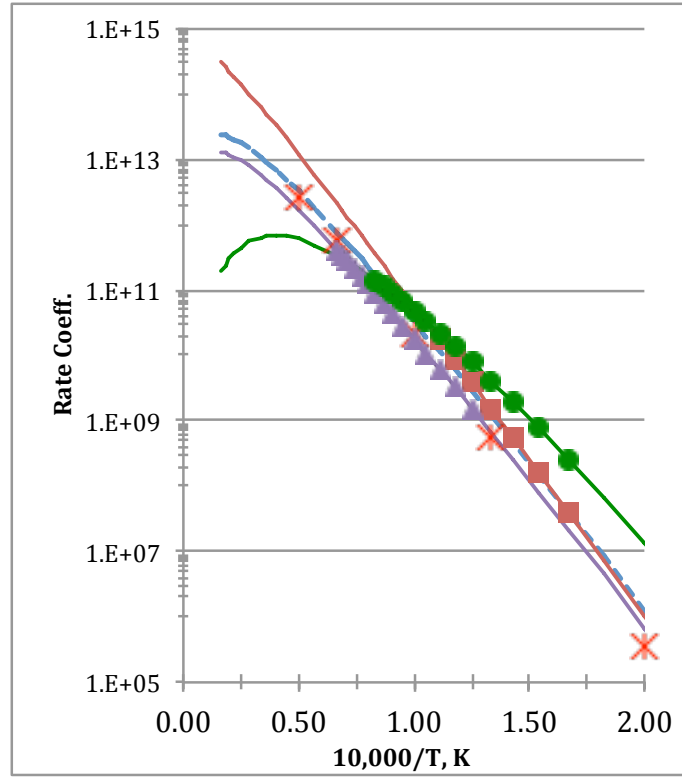
Figure 11: Thermal rate coefficients for $N_2$ dissociation resulting from $N_2 + N_2$ collisions. The QCT results (red asterisks) are compared with the rate coefficients determined from shock tube experiments: Byron (Ref. [?]) brown squares, Appleton (Ref. [?]) purple triangles, and Hanson (Ref. [?]) green circles. For the shock tube results, the symbols span the range of temperatures determined in the particular experimental studies and the lines represent extrapolation of the fitted rate coefficient. The dashed blue line represents the rate coefficient in the Park model (Ref. [?, ?]).

with a one-dimensional flow solver. The system of equations is solved for conditions expected for reentry into Earth's atmosphere at 10 km/s. Although extremely accurate, the ro-vibrational state-to-state approaches can only be applied to zero and one-dimensional problems owning to their large computational cost. Thus, in order to extend their applicability to multi-dimensional flow conditions, reduced order model must be constructed. To this aim, a coarse grained model is proposed by lumping the ro-vibrational energy levels into a smaller number of bins. The results obtained by means of the full ro-vibrational collisional model are compared to those obtained by means of a vibrational collisional model.

## 4.1 Kinetic Processes included in the Models

The NASA Ames database[?, ?, ?, ?], that includes the rate coefficients described in Section 3.1, comprises a complete and self-consistent set of thermodynamic and kinetic data needed to describe the elementary state-to-state kinetics of $N_2$-N and $N_2$-$N_2$ interactions. While the analysis carried out in this work is restricted to the study of $N_2$-N relaxation, an ongoing effort addresses the study of dynamics of the $N_2$-$N_2$ system.

The database includes 9390 ro-vibrational energy levels $N_2(v, J)$ for the electronic ground-state of nitrogen, where index $v$ stands for the vibrational quantum number, and index $J$, the rotational quantum number. These levels can also be sorted by increasing energy and denoted by means of a global index $i$. The relation between the $i$ and $(v, J)$ notations is expressed as

$$i = i(v, J), \quad v = 0, \ldots, v_{\max}, \quad J = 0, \ldots, J_{\max}(v),$$

and conversely by the relations

$$v = v(i), \quad J = J(i), \quad i \in \mathcal{I}_{\mathrm{BP}},$$

where $\mathcal{I}_{\mathrm{BP}}$ is the set of global indices for the nitrogen energy levels. The ro-vibrational energy levels were determined using quantum mechanics calculations within the WKB approximation, [?] using the recently developed $N_2(X^1\Sigma_g^+)$ potential of LeRoy *et al.*[?] There are 61 vibrational levels ($v = 0$ to 60) for the rotation-less ($J=0$) potential and for $v = 0$ the maximum rotational quantum number is 279. Most of these levels (7421) are bound, *i.e.*, their energy is lower than the dissociation energy relative to the ($v = 0, J = 0$) level, equal to 9.75 eV for the electronic ground-state of molecular nitrogen, the remaining levels are pre-dissociated, or quasi-bound, *i.e.*, their energy is higher than the dissociation energy relative to the level ($v = 0, J = 0$), but lower than the $J$ dependent centrifugal barrier. The bound energy levels are denoted by the set $\mathcal{I}_{\mathrm{B}}$, and the pre-dissociated energy levels, by the set $\mathcal{I}_{\mathrm{P}}$, with $\mathcal{I}_{\mathrm{B}} \cup \mathcal{I}_{\mathrm{P}} = \mathcal{I}_{\mathrm{BP}}$ and $\mathcal{I}_{\mathrm{B}} \cap \mathcal{I}_{\mathrm{P}} = \emptyset$. The total wave function for the nitrogen molecule must be symmetric with respect to exchanging the nuclei (Bose-Einstein statistics), the degeneracy of the energy levels is given by the expression $g_i = (2J(i) + 1)g_i^{NS}$, $i \in \mathcal{I}_{\mathrm{BP}}$, where the nuclear spin degeneracy is $g_i^{NS} = 6$ for even $J(i)$ and $g_i^{NS} = 3$ for odd $J(i)$.

The database for the $N_2 + N$ system comprises more than 20 million reactions in total for three types of processes: collisional dissociation of bound states and pre-dissociated states,

$$N_2(i) + N \underset{k_i^{Db}(T)}{\overset{k_i^{Df}(T)}{\rightleftarrows}} N + N + N, \quad i \in \mathcal{I}_{\mathrm{BP}}, \tag{54}$$
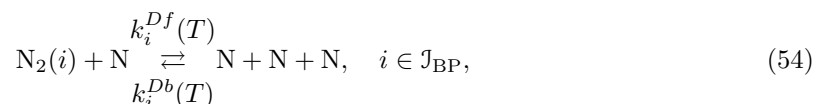
pre-dissociation, or tunneling, of pre-dissociated states,

$$\text{N}_2(i) \underset{k_i^{Pb}(T)}{\overset{k_i^{Pf}}{\rightleftarrows}} \text{N} + \text{N}, \quad i \in \mathcal{I}_\text{P}, \tag{55}$$

and collisional excitation between all states,

$$\text{N}_2(i) + \text{N} \underset{k_{ji}^{E}(T)}{\overset{k_{ij}^{E}(T)}{\rightleftarrows}} \text{N}_2(j) + \text{N}, \quad i,j \in \mathcal{I}_\text{BP}, \quad j > i. \tag{56}$$

The collisional excitation processes include the contribution of both inelastic (non-reactive) and exchange processes

$$k_{ij}^{E}(T) = k_{ij}^{IE}(T) + k_{ij}^{EE}(T). \tag{57}$$

The first term $k_{ij}^{IE}(T)$ accounts for the contribution due to inelastic processes, where kinetic energy is transferred into internal energy during the collision. The second term $k_{ij}^{EE}(T)$ accounts for exchange processes and the transfer between kinetic and internal energies occurs via substitution of one bounded atom of the molecule with the colliding partner. The importance of this elementary process on the kinetics of dissociation is discussed later in this section.

The cross sections for these reactions are computed using the QCT method as previously described. The direct reaction rate coefficients $k_i^{Df}(T)$, $k_i^{Pf}(T)$, and $k_{ij}^{E}(T)$, $j > i$, used in the present work, are obtained from these cross sections at nine values of the gas translational temperature $T$ between 7500 and 50,000 K, from these cross-sections.[?, ?] Reverse rate coefficients result from micro-reversibility of the processes among the energy levels Ei, $i \in \mathcal{I}_\text{BP}$, yielding the following expressions for the equilibrium constants for collisional dissociation of truly bound states and pre-dissociated states,

$$K_i^{D}(T) \;\; = \;\; \frac{k_i^{Df}(T)}{k_i^{Db}(T)} = \frac{[g_\text{N} Q_\text{N}^t(T)]^2}{g_i Q_{\text{N}_2}^t(T)} \exp\left(\frac{-(2E_\text{N} - E_i)}{k_\text{B} T}\right), \quad i \in \mathcal{I}_\text{BP}, \tag{58}$$

pre-dissociation, or tunneling, of pre-dissociated states,

$$K_i^{P}(T) \;\; = \;\; \frac{k_i^{Pf}(T)}{k_i^{Pb}(T)} = \frac{[g_\text{N} Q_\text{N}^t(T)]^2}{g_i Q_{\text{N}_2}^t(T)} \exp\left(\frac{-(2E_\text{N} - E_i)}{k_\text{B} T}\right), \quad i \in \mathcal{I}_\text{P}, \tag{59}$$

and collisional excitation between all states.

$$K_{ij}^{E}(T) \;\; = \;\; \frac{k_{ij}^{E}(T)}{k_{ji}^{E}(T)} = \frac{g_j}{g_i} \exp\left[\frac{-(E_j - E_i)}{k_\text{B} T}\right], \quad i,j \in \mathcal{I}_\text{BP}, \quad j > i, \tag{60}$$

where symbol $k_\text{B}$ stands for Boltzmann's constant. The translational partition functions are defined as

$$Q_{\text{N}_2}^t(T) = \left(\frac{2\pi k_\text{B} m_{\text{N}_2} T}{h_\text{P}^2}\right)^{3/2}, \quad Q_\text{N}^t(T) = \left(\frac{2\pi k_\text{B} m_\text{N} T}{h_\text{P}^2}\right)^{3/2}, \tag{61}$$

where symbol $h_P$ stands for Planck's constant. The nitrogen atom degeneracy is $g_N = 12$ (nuclear and electronic spin contributions).

The total number of possible combinations for collisional excitation exceeds 44 million processes and the number of non-zero rate coefficients in the database exceeds 19 million. The remaining transitions have very small probabilities, because they are transitions with large activation energy (*i.e.*, $E_j \gg E_i$) or are forbidden by quantum mechanical arguments (inelastic transitions for which $\Delta J$ is odd). Notice that both endothermic (excitation) and exothermic (de-excitation) processes are found in the database. The number of exothermic processes with non-zero rate coefficient, (13.5 million), is larger than the number of endothermic processes (7.1 million). A small number of transitions (about 1.5 million) have rate coefficients for both types of processes in the database. In this case, the exothermic rate coefficients are preferentially used, since the QCT method should give more reliable results in this direction. In general, we have observed that the endothermic rate coefficients agree within 70 % of the quantities computed by means of the exothermic rate coefficients using micro-reversibility. These discrepancies are due to differences in the statistical sampling errors of the QCT calculations between direct and reverse processes. We have found the results of the master equation calculations to be insensitive to the rate coefficients selected when data from both processes are available.

## 4.2 Master equations

We wish to investigate the behavior of nitrogen molecules in their electronic ground state undergoing dissociation, when subjected to sudden heating in an ideal chemical reactor. We make the following assumptions:

- The reactor is plunged into a thermal bath maintained at constant temperature $T$.

- The initial number density of the gas inside of the reactor is set to $n=2.4\times10^{24}$ [m$^{-3}$]. For this value, the translational energy mode of the atoms and molecules is assumed to follow a Maxwell-Boltzmann distribution at the temperature $T$ of the thermal bath. This is equivalent to an initial pressure of 10,000 [Pa].

- At the beginning of the numerical experiment, the population of the ro-vibrational energy levels is assumed to follow a Maxwell-Boltzmann distribution at the internal temperature $T_0^I$ = 300 K.

- The volume of the chemical reactor is kept constant during the experiment and the thermo-dynamic system is closed (no mass exchange with surrounding environment).

- The electronic excitation and ionization processes are neglected. Dissociation and excitation processes by molecular nitrogen impact are assumed to be negligible with respect to the processes induced by atomic nitrogen impact. This assumption is justified given the initial concentration of atomic nitrogen equal to the non-equilibrium molar fraction value $x_N=5\%$.

The rotation and vibration of molecules of a gas can be described by means of a kinetic approach. The temporal evolution of the populations of molecules in a particular ro-vibrational energy level $(v,J)$ is then obtained by solving a system of master equations. It comprises the following species continuity equations for the nitrogen atom and the rovibrational energy levels of molecular nitrogen

$$\frac{\mathrm{d}}{\mathrm{d}t}n_{\mathrm{N}} = 2\sum_{i\in\mathcal{I}_{\mathrm{BP}}}\dot{\omega}_i^D + 2\sum_{i\in\mathcal{I}_{\mathrm{P}}}\dot{\omega}_i^P, \tag{62}$$

$$\frac{\mathrm{d}}{\mathrm{d}t}n_i = -\dot{\omega}_i^D + \dot{\omega}_i^E, \quad i\in\mathcal{I}_{\mathrm{B}}, \tag{63}$$

$$\frac{\mathrm{d}}{\mathrm{d}t}n_i = -\dot{\omega}_i^D - \dot{\omega}_i^P + \dot{\omega}_i^E, \quad i\in\mathcal{I}_{\mathrm{P}}, \tag{64}$$

where quantity $n_{\mathrm{N}}$ is the atomic nitrogen number density, and $n_i$, the number density of level $i$. The chemical production rates for the processes of collisional dissociation, $\dot{\omega}_i^D$, pre-dissociation, $\dot{\omega}_i^P$, and collisional excitation, $\dot{\omega}_i^E$, are given by the expressions

$$\dot{\omega}_i^D = n_{\mathrm{N}}k_i^{Df}(T)\left[n_i - \frac{1}{K_i^D(T)}(n_{\mathrm{N}})^2\right], \quad i\in\mathcal{I}_{\mathrm{BP}}, \tag{65}$$

$$\dot{\omega}_i^P = k_i^{Pf}(T)\left[n_i - \frac{1}{K_i^P(T)}(n_{\mathrm{N}})^2\right], \quad i\in\mathcal{I}_{\mathrm{P}}, \tag{66}$$

$$\dot{\omega}_i^E = -n_{\mathrm{N}}\sum_{\substack{j\in\mathcal{I}_{\mathrm{BP}}\\j<i}} k_{ji}^E(T)\left[\frac{1}{K_{ij}^E(T)}n_i - n_j\right] - n_{\mathrm{N}}\sum_{\substack{j\in\mathcal{I}_{\mathrm{BP}}\\j>i}} k_{ij}^E(T)\left[n_i - \frac{1}{K_{ij}^E(T)}n_j\right], \quad i\in\mathcal{I}_{\mathrm{BP}} \tag{67}$$

The master equations allow for the simulation of an isochoric reactor plunged into a thermal bath. The initial $n_i$ populations follow a Maxwell-Boltzmann distribution at the internal temperature $T_0^I = 300\ K$. Due to its stiffness, the system of coupled ordinary differential eqs. (62-64) is solved using the backward differentiation method [?] implemented in the LSODE package.[?] Notice that the pressure can be calculated at any time by means of the relation $p = nk_{\mathrm{B}}T$, with the mixture number density $n = n_{\mathrm{N}_2} + n_{\mathrm{N}}$.

## 4.3   Results: Energy transfer and dissociation kinetics

In this section, the rovibrational collisional model, describing the detailed kinetics in the isothermal and isochoric reactor, is used to the study of energy transfer and dissociation processes for a wide range of conditions. Three observables are calculated and discussed: internal relaxation times, a global dissociation rate, and the coupling of dissociation and internal energy excitation.

Insights in the dynamics of the relaxation can be obtained by the analysis of the time evolution of the rotational and vibrational temperatures, shown in Fig. (12 a). The behavior of the excitation process is sensitive to the temperature excitation drastically depends on the temperature of the heat bath, $T$. At low temperature (*e.g.*, $T = 5{,}000$-$10{,}000$ K), the time response of the rotational energy modes appears to be significantly faster than vibration. This behavior is not surprising and the differences in the time-response of the rotational manifold at low temperature is well documented in literature. The internal temperature sits in between the two other temperatures, thus yielding an inadequate description of the internal excitation of the internal manifold. The relaxation of the gas at higher temperatures (*e.g.*, $T = 30{,}000$ K) is profoundly different. Vibrational and rotational temperatures relax at the same rate, thus implying the existence of a unique internal temperature.

The situation described here is often encountered in the post relaxation region behind a strong shock during high speed atmospheric entry. In this situation, conventional physical models assume a fast equilibration of rotation and translational temperature, while the vibrational temperature is assumed to relax at much lower rate. The results here presented clearly demonstrate that this assumption is not valid. At intermediate temperatures (*e.g.*, $T = 15,000$ to 20,000 K), relaxation of rotation is to some extent faster than vibration, with the internal temperature being a fairly good indicator of the process.
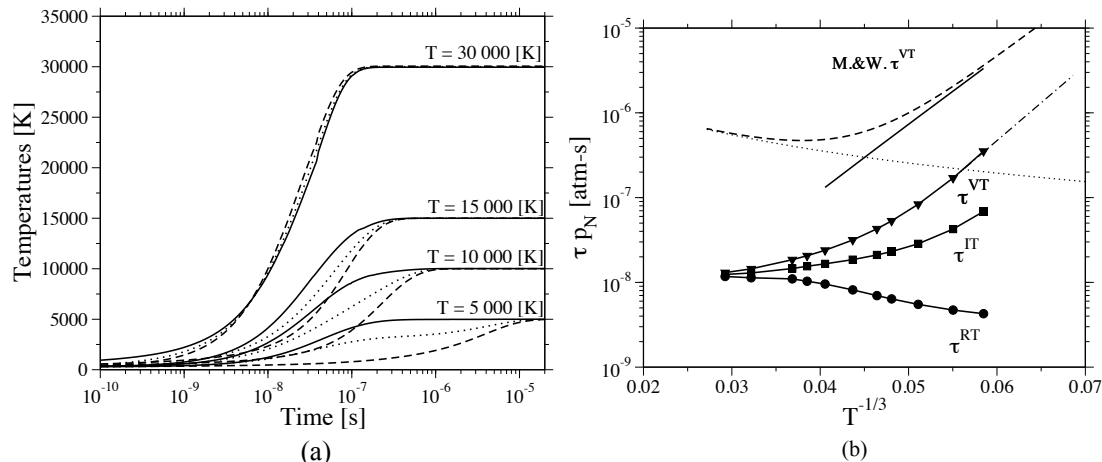


Figure 12: **(a) Thermal relaxation studies for constant temperature heat-bath for different kinetic temperatures. Rotational temperatures are represented by unbroken lines, while the vibrational temperatures are indicated with broken lines. Dissociation processes are not considered. (b) Comparison of the *ab-initio* relaxation time $\tau_{VT}$ against the Millikan-White correlation formula.[?] The dotted line is the limiting high temperature correction proposed by Park. In the same figure, $\tau_{RT}$ and $\tau_{IT}$ are shown as a function of the kinetic temperature. Dissociation processes are not considered.**

The analysis of the time evolution of the various temperatures suggests the possibility of describing the relaxation processes by using the simple linear relaxation model proposed by Landau and Teller.[?, ?] The characteristic relaxation extracted are shown in Fig. (12b). To the best of our knowledge, there is no experimental data on the relaxation of $N_2$-N systems. Most of the experiments available in literature focus on the vibrational relaxation of nitrogen molecules with other collision partners (*e.g.*, $N_2$, Ar, $O_2$ ...).[?] In the 1960s, Millikan and White[?] generated empirical correlation formulas to describe the behavior of the relaxation times as a function of the heat bath temperature. These formulas are often applied to the description of the relaxation of diatomic molecules for which experimental data are not available. In Fig. (12b), we compare the relaxation times for vibrational, rotational and internal relaxation with the correlation formula introduced by Millikan and White.[?] At high temperatures, the Millikan and White relaxation time has been corrected to account for the limiting of the excitation rates, as suggested by Park.[?] The direct comparison of the vibrational relaxation ($\tau^{VT}$) shows similar temperature dependence $T^{-1/3}$, although the absolute value of the relaxation time seems to be shorter at least by one order

of magnitude. At low temperatures ($T < 15,000$ [K]), the characteristic relaxation times for rotation are significantly lower than the vibrational and internal relaxation times. The large disparity in relaxation times observed a low temperatures disappears at the higher temperatures as all the relaxation times converge to a common asymptote.

The evolution of the rovibrational energy populations of the nitrogen molecule are depicted in Fig. (13) as a function of the level energy at various times of the relaxation. In the early stages of the numerical simulation, the bulk of the nitrogen molecules occupy the lower ro-vibrational energy levels. Over 99% of the molecules is found in the ground vibrational state and only the low lying rotational levels ($J < 25$) are significantly populated. With time, the random motion of molecules and atoms brings about collisions, thus enabling the transfer of kinetic energy into rotational and vibrational energy. Initially, the population of the internal levels strongly depart from equilibrium condition and the dynamics of each level is governed by its own kinetics. The low lying levels are at frozen at $T_0^I$ and the population of higher levels steadily increases, displaying a characteristic "banana shape". By $10^{-8}$ s, the high-lying levels are nearly at T, even if the distribution is still fairly broad. The experimental results of Robben and Talbot[**?**] confirmed a similar behavior for the relaxation of pure nitrogen gas behind a strong shock wave. Robben and Talbot "found that it was possible to represent their results approximately by the merging of two rotational distribution function corresponding to the temperatures upstream and downstream of the shock wave." As the relaxation proceeds further, *e.g.*, t=$10^{-7}$, part of the gas reaches a state of partial equilibrium (shown in red symbols), during which the population is dissected into separate strands for each low-lying $v$, while the high-lying levels have already thermalized at the heat bath temperature, $T$. This is a manifestation of the faster equilibration of rotation at lower temperatures. The entire relaxation process takes up to 1 $\mu$s. At this time, the population of the internal levels has relaxed to the final Maxwell-Boltzmann distribution at heat bath temperature, $T = 10,000$ [K] (shown in blue).

In the early times of the simulation, the dynamics of the populations of the bound states and part of the quasi-bound is not influenced by dissociation. Thus, close to 1 $\mu$s, when the dissociation becomes significant (blue symbols), the distribution is already very close to equilibrium. This behavior is characteristic of low temperature relaxation: at these conditions, dissociation and relaxation are two distinct processes and the energy transfer process is almost completed before the onset of dissociation. Departures from the Maxwell-Boltzmann distribution are limited the high lying states close to the dissociation and the quasi-bound states. During the incubation period, part of the quasi-bound levels are already depleted, owing to their short lifetime.

At higher temperatures ( T > 10,000 - 15,000 [K]), dissociation occurs while the internal structure of the gas is not completely relaxed to the heat bath temperature. At 30,000 [K] significant dissociation occurs only after 0.01 $\mu$s, when a bit less then half of the equilibration energy has been transferred to the rotational and vibrational energy modes.

The global dissociation rate coefficient, $k^D$, defined as

$$\sum_{i \in \mathcal{I}_{\mathrm{BP}}} \dot{\omega}_i^D = k^D(T) \ n_{\mathrm{N}_2} n_{\mathrm{N}}. \tag{68}$$

changes with time throughout the relaxation, as shown in Fig. (14a). This is due to the fact that the state specific rate coefficients of each ro-vibrational level differ and the distribution of the molecules in the ro-vibrational levels change with time. Only when the system reaches the QSS condition it
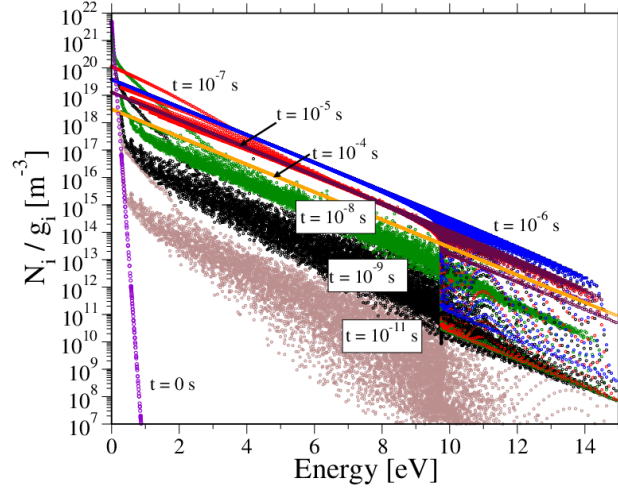
Figure 13: **Normalized population distribution function ($N_i/g_i$) for different times in the relaxation: t = 0 in violet; t = $10^{-11}$ s in brown; t = $10^{-9}$ s in black; $10^{-8}$ s in green; $10^{-7}$ s in red; $10^{-6}$ s in blue; $10^{-5}$ s in maroon; $10^{-4}$ s in orange. The heat bath temperature is 10,000 K.**

is possible to define a meaningful global rate coefficient, because the relative populations do not change appreciably. Thus, the plateau in the time evolution of $k^D$ is used to define the reaction rate coefficient. This method was firstly proposed by Bourdon *et al.*[?] for the estimation of the ionization rate coefficient of nitrogen atoms. At low temperature the time required to establish a
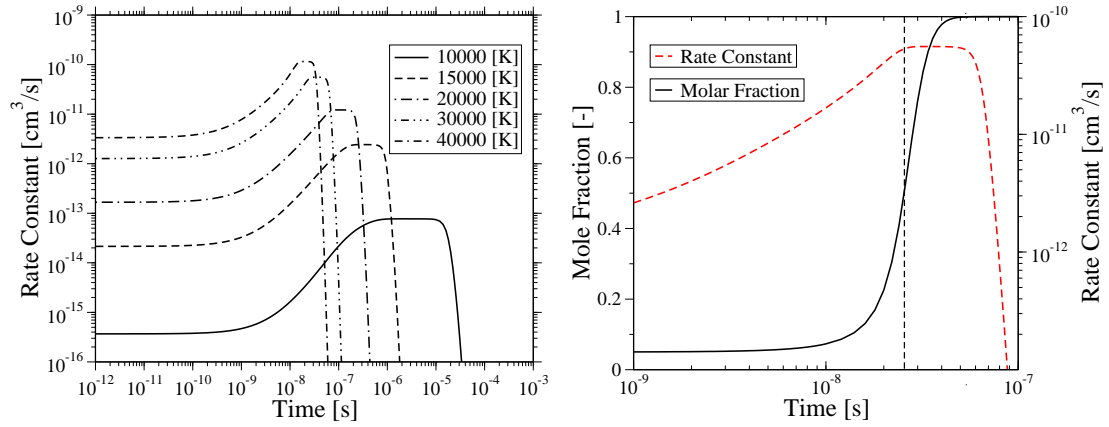


Figure 14: **(a) Estimation of the instantaneous global rate coefficient for dissociation as function of the kinetic temperature. (b) Atomic nitrogen mole fraction (black unbroken line) and instantaneous rate coefficient (red dashed lines) as a function of time for a heat bath temperature of 30,000 [K].**

QSS distribution is larger then the time needed to the onset of dissociation. As the temperature increases, the QSS distribution is established only when significant part of molecules have dissociated. This is clearly shown in Fig. (14b). At 30,000 [K], the population reaches the QSS condition and over 50 % of the nitrogen molecules are already completely dissociated. In this case the $k^D$ cannot be used to describe the global dissociation of nitrogen molecules, thus loosing its meaning.

In Fig. (15a), the dissociation rate $k^D$ as a function of temperature is compared against the experimental data by Appleton *et al.*[?] The agreement between predicted and experimental data is excellent. In the same figure, we have included the rate coefficients obtained by averaging the state specific rates with a Maxwell-Boltzmann distribution, $k^{D\star}$, referred to as the thermal rate coefficient in the following. As expected the assumption of equilibrium leads to an overestimation of the dissociation rate coefficient, since the thermal rates does not account for the distortion in the tail of the distribution due to dissociation. The influence of pre-dissociation on the rate coefficient appears negligible, while the exchange processes significantly affect the global dissociation reaction rate. If exchange processes are neglected, the dissociation rate is underestimated by a factor 2-3.
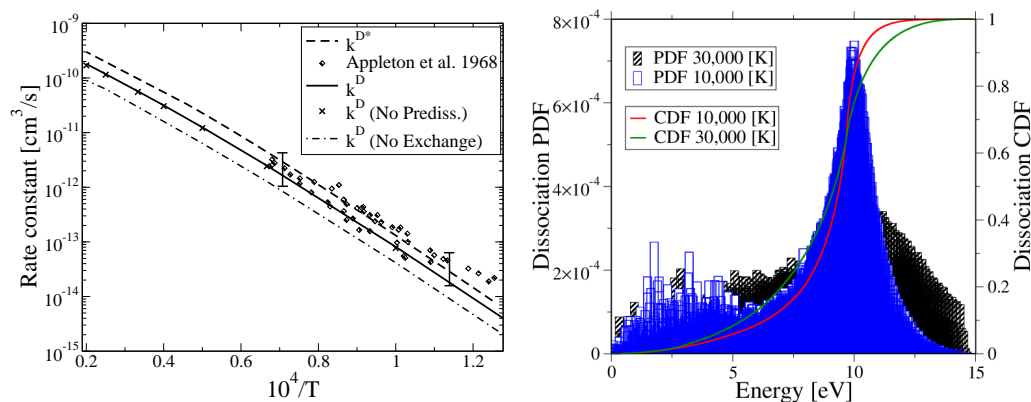


Figure 15: **(a) Comparison of the global rate coefficient for dissociation with experimental value from Appleton *et al.*.[?] In the same figure: the thermal rate $k^{D\star}$ is presented in broken line; Diamonds symbols refer to the experimental data; The remaining curves were obtained by the solution of the master equations: the unbroken line curve includes all the processes. The cross symbols do not include the pre-dissociation processes, while the dash-dotted line includes all the processes with the exception of exchange reactions. (b) Dissociation probabilities (PDFs) as a function of the energy level in the midst of the QSS regions. The blue bars refer to the low temperature case (10,000 K) at t $= 8 \times 10^{-6}$. The black bars refer to the high temperature case (30,000 K) at t $= 3 \times 10^{-8}$. The cumulative distribution functions (CDFs) for the low and high temperature cases are represented by the red and green curve respectively.**

More insight into the dynamics of dissociation can be revealed from the analysis of the dissociation probability density function (PDF) and the cumulative distribution function (CDF). The PDF is defined as

39

$$p(E_i) = \frac{k_i^{Df}(T)n_i n_N}{k^D(T)}. \tag{69}$$

and the CDF is defined as the cumulative sum (or integral in the continuous case) of the PDF. Thus, the value of the CDF accounts for the contribution (in percentage) of the energy levels with energy lower and equal to a given energy level, to the total dissociation rate coefficient. The dissociation PDFs and CDFs, in Fig. (15b), show a small number of low-lying levels with a large PDF value. Given their reduced number, these levels do not contribute significantly to the dissociation rate coefficient (levels $< 5$ eV contributes less than 10% at 30,000 [K]), thus demonstrating the existence of preferential mechanism in dissociation. According to this mechanism the dissociation of molecular species is favored by the ro-vibrational excitation. Thus, the molecules in the higher ro-vibrational levels are assumed to be preferentially dissociated. This phenomenon has been extensively studied in literature without any clear conclusion. The dissociation probabilities for 10,000 and 30,000 [K] clearly show that the most of the dissociation comes from the high lying vibrational, internal and rotational energy levels. Some differences can be observed when comparing the low and high temperature heat baths. In the lower temperature case, about 80 % of dissociation comes from the bound levels in the energy range 8-10 [eV]. At the higher temperature, the distribution is more uniform and the contribution from the same levels is only about 40-50 %. About 30 % of the dissociation comes from the lower levels and the rest from the quasi-bound levels. Given the important contribution to the dissociation coming from the upper part of the distribution, the correct prediction of the population of the high-lying states become important for the correct modeling of the dissociation process.

The analysis of the results, obtained through the solution of the master equation, put forward the differences in the dynamics of low lying, intermediate and high-lying (bound and quasi-bound) levels. The population of the low lying vibrational levels can be approximated by a series of Maxwell-Boltzmann distributions at a rotational temperature $T^R(v)$, where the temperature of each vibrational level monotonically increases with the vibrational quantum number.[?] The population of the intermediate and high lying bound levels quickly thermalize at the common temperature close to the heat-bath kinetic temperature, thanks, in large part, to the contribution of the exchange processes. Substantially different is the behavior of quasi-bound levels that can be further classified in long and short lived, depending on their widths, $k_i^{Pf}$. Long lived levels constitute significant part of quasi-bound levels and due to their small widths, have a non-negligible influence on the relaxation process. During the entire relaxation, their population distribution strongly departs from a thermal distribution, owing to the large dissociation rate coefficients, $k_i^{Df}$. The short lived quasi-bound states are strongly depleted due to their large widths and can be safely neglected, since they play a very small role in the relaxation.

The dynamics of relaxation strongly varies with the kinetic temperature of the heat-bath: At low temperature, the rotational relaxation is very fast and the rotational and translational energy modes quickly equilibrates, while vibration lags behind. At high temperature, rotational and vibrational temperatures relax at the same rate, thus justifying the existence of a common internal temperature. Thus, the assumption of fast thermalization of the rotational manifold at the heat bath temperature $(T = T^R)$ appears questionable in strong non-equilibrium conditions. Across all the temperature range, rotational and vibrational relaxation can be well approximated by a simple Landau-Teller formula, provided that the phenomenological relaxation times are fitted using the solution of the

full master equation.

# 5  Coarse Grained Model

The unprecedented level of physical realism achieved by the *ab-initio* computations in the characterization of the interaction of colliding particles allows for the complete description of the non-equilibrium state of the gas by tracking the individual rotational and vibrational states.

In practice, however, the determination of the population of each internal state of every particle in the flow is unfeasible, given the extremely large number of excited states and excitation pathways in the gas. The study of the ro-vibrational kinetics quickly becomes intractable even in 0D simulations! The huge amount of information provided by *ab-initio* calculations has great value, but it must be tailored and synthesized to fulfill the needs of practical hypersonic flow problems. Thus, it is imperative that *reduced-order models* be developed.

## 5.1  Theory

Substantial reduction of the computational effort can be obtained by using a coarse grained model to represent the kinetics of the internal states of atoms and molecules. The approach consists of three steps:

1. grouping of the internal energy levels

2. reconstruction of the level population of each internal energy mode and derivation of the group averaged quantities, *e.g.* reaction rate constants.

3. solution of the master equation

**Energy Grouping:**  The large number of internal levels of atoms and molecules requires the knowledge of a huge number of kinetic parameters, describing the elementary processes occurring in a reacting gas. Often, however, the calculation of these parameters is unfeasible (*e.g.*, $N_2$-$N_2$) or extremely time consuming. Furthermore, the description of the dynamics of each individual level of atoms and molecules in the gas is not required, since often times is the description of macroscopic processes (*e.g.*, energy transfer) that matters or at most a coarse description of the internal distribution function. A major reduction in the computational complexity of the problem can be obtained by grouping the internal levels of similar energy into groups, thus filtering out dynamically irrelevant degrees of freedom. The grouping is obtained by subdividing the internal energy space into multiple groups, similar to the grid cells or elements used in the physical space in CFD. However, the subdivision here is more flexible. It can be based on the values of energy levels, or vibrational and rotational quantum numbers.

**Population Reconstruction:**  The population of the ro-vibrational energy levels grouped in the energy bins can be easily obtained, once the bin distribution is specified. In this work, it is assumed that the population of the energy levels within each bin follows a Boltzmann distribution at the local translational temperature $T$:

$$\frac{n_i}{\tilde{n}_k} = \frac{g_i}{\tilde{Q}_k(T)} \exp\left(-\frac{\Delta \tilde{E}_k(i)}{k_B T}\right), \quad i \in I_k, \quad k \in K_{BP}, \tag{70}$$

where the number density $\tilde{n}_k$ and the partition function $\tilde{Q}_k(T)$ of the energy bin $k$ in Eq. (70) are defined as:

$$\tilde{n}_k = \sum_{i \in I_k} n_i, \tag{71}$$

$$\tilde{Q}_k(T) = \sum_{i \in I_k} g_i \exp\left(-\frac{\Delta \tilde{E}_k(i)}{k_B T}\right), \quad k \in K_{BP}. \tag{72}$$

The assumption of local equilibrium of the internal levels within each bin is justified by the large reaction rate coefficients for excitation and de‑excitation which characterize groups of levels with similar internal energy. This assumption is found to work quite well in the condition of interest to this work as shown in Section (5.2). Furthermore, increasing the number of energy bins can easily extend the range of validity of this model to stronger non‑equilibrium conditions.

**Solution of the Master Equation:**  The group densities $\tilde{n}_k$ in Eq. (72) constitute the unknowns of the mathematical problem to be solved. The governing equations are obtained by summing the master equations of the ungroup system over the states within each group. Thus, the system of equations can be expressed as follows:

$$\sum_{i \in \mathcal{I}_k} \frac{d}{dt} n_i = \frac{d}{dt} \tilde{n}_k = \overbrace{\sum_h \sum_{i \in \mathcal{I}_k} \sum_{j \in \mathcal{I}_h} (-k_{ij} n_i n_N + k_{ji} n_j n_N)}^{\text{Chemical Source term}} + \ldots = \sum_h -\tilde{k}_{kh} \tilde{n}_k n_N + \tilde{k}_{hk} \tilde{n}_h n_N \tag{73}$$

where the generic $k$ and $h$ groups are indicated with $\mathcal{I}_k$ and $\mathcal{I}_h$. The state-specific reaction rate coefficients are indicated with $k_{ij}$, and the group-averaged rate coefficients with $\tilde{k}_{kh}$. The Equations (73) constitute a system of non-linear ODE and can be solved numerically.

## 5.2  Shock Tube Heated Flows

In this section, we apply the coarse grained model previously discuss to the modeling of the thermo-chemical relaxation behind a strong shock wave. The non-equilibrium flow behind a normal shock wave is computed under the following assumptions: i) The flow is steady and one-dimensional; ii) The flow is inviscid; iii) and the shock wave moves at constant speed.

The flow problem is conveniently studied in the shock reference frame. The shock front is treated as a mathematical discontinuity, in that the flow quantities experience a discrete jump, when crossing the shock. The governing equations for the problem under investigation are the steady, one-dimensional Euler equations. The flow-field behind the shock is obtained by solving numerically the governing equation. The solution initial value is obtained by means of the Rankine-Hugoniot jump relations (with the assumption of frozen dissociation and excitation within the shock). The population of the ro-vibrational levels immediately behind the shock is assumed
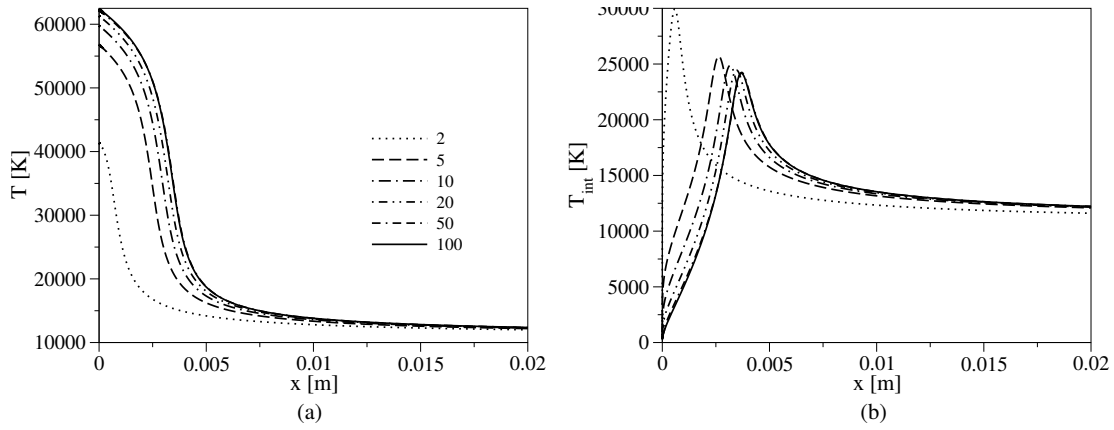
Figure 16: **(a) Bin number convergence study on: (a) the translational temperature (b) the internal temperature. Spatial evolution behind the shock wave.**

to follow a Maxwell-Boltzmann distribution. A detailed description of the governing equations for the inviscid shock test-case are given in literature.[**?, ?**]
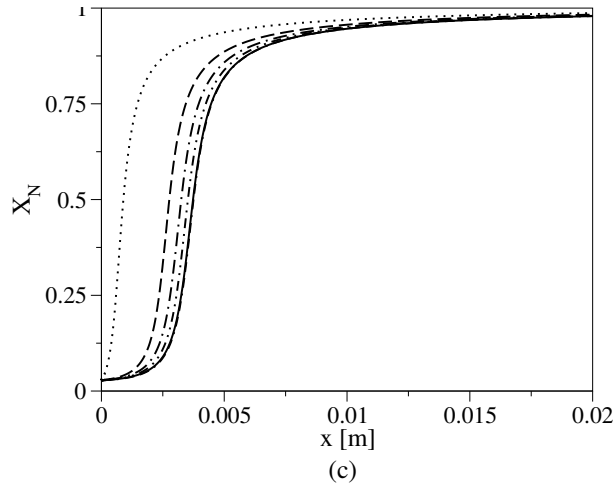


Figure 17: **Bin number convergence study on mole fraction evolution behind the shock wave.**

Figure (16) and (17) show the evolution of the temperatures and the N atom mole fraction behind the shock wave for different number of energy bins. The numerical solution obtained when using 2 and 5 bins tends to overestimate the dissociation rate, implying that a larger number of groups should be used. It should be mentioned that this behavior could be partly due to the lower value of the post-shock temperature (especially for the 2 energy bins case). The accuracy improves, as expected, when the number of energy bins is increased. For the calculations shown in Fig. (16)

and (17), the differences between the 50 and 100 energy bin solutions are barely noticeable. A further increase of the number of energy bins does not induce appreciable changes in the solution. The dissociation dynamics is already well captured with only 20 energy bins. A larger number of bins would certainly allow for a more accurate description of the dynamics of the elementary levels at the cost of a more expensive calculation and a more complex physical model. It is worth mentioning that the cost of the numerical simulation scales with the square of the number of pseudo-species included in the model.

# 6    Concluding Remarks

In this chapter we make a very detailed discussion of non-equilibrium effects that are important for hypersonic earth entry. We start from first principles, solving the quantum mechanical equations of motion for electrons and nuclei. We show how the separation of electronic and nuclear motion is achieved, and give practical procedures for obtaining accurate analytic representations of the potential energy surfaces. We discuss in detail the issues involved in solving for the nuclear motion and the trade-offs one must make to move forward.

Now in the universe that consists of two particles, N and $N_2$ or $N_2+N_2$, the observable quantity is the cross section for a transition from initial state $i$ to final state $f$, and this can be straightforwardly computed using the steps described above. In the macroscopic world, however, where there are many, many particles (recall there are $6.0\times10^{23}$ particles in a mole), and the time evolution of a population distribution is governed, in 0-d, by the Master equation. This requires the cross sections for all possible initial and final states. For the $N_2$ molecule, there are 9390 possible $v, J$ levels. This makes solving the Master a very arduous task, and in order to accurately couple non-equilibrium effects to CFD or DSMC calculations, one needs a reliable, vastly simplified model.

We have used our comprehensive database of cross-sections for the $N+N_2$ system to carry out a series of benchmark calculations of the non-equilibrium effect in 0-d or 1-d by solving the full Master equation. We have then carefully analyzed the results as a function of propagation time, not only for Macroscopic quantities like the internal temperature, but for individual state populations. This is led us to develop and test new models for accurately reproducing the results of the full Master equation but at a very small fraction of the cost. We find that a fairly small number of bins can well reproduce the results of the full 9390 coupled state problem. This is a very encouraging result, for this is such a simple approximation. We fully expect that more sophisticated models can be developed that will improve the situation even further.

# References

[1] Park, C. *Nonequilibrium Hypersonic Aerothermodynamics*; J. Wiley, New York, 1990.

[2] Park, C. *J. Spacecraft and Rockets* **1985**, *22*, 27–36.

[3] Park, C.; *A Review of Reaction Rates in High Temperature Air*; AIAA Paper AIAA-89-1740; 1989.

[4] Park, C. *J. Thermophys. Heat Trans.* **1988**, *2*, 8–16.

[5] Park, C. *J. Thermophys. Heat Trans.* **1989**, *3*, 233–244.

[6] Park, C.; Howe, J.; Jaffe, R.; Candler, G. *J. Thermophys. Heat Trans.* **1993**, *7*, 385–398.

[7] Park, C.; Jaffe, R.; Partridge, H. *J. Thermophys. Heat Trans.* **2001**, *15*, 76–90.

[8] Johnston, C.; Brandis, A.; Sutton, K.; *Shock Layer Radiation Modeling and Uncertainty for Mars Entry*; AIAA Paper AIAA-2012-2866; 2012.

[9] Brandis, A.; Johnston, C.; Cruden, B.; Prabhu, D.; *Investigation of Nonequilibrium Radiation for Mars Entry*; AIAA Paper AIAA-2013-1055; 2013.

[10] Laganà, A.; Garcia, E.; Ciccarelli, L. *J. Phys. Chem.* **1987**, *91*, 312–314.

[11] Billing, G. D. *Computer Phys. Rep.* **1984**, *1*, 237–296.

[12] Laganà, A.; Garcia, E. *J. Phys. Chem.* **1994**, *98*, 502–507.

[13] Longo, N. F.; Laganà, A.; Garcia, E.; Gimenez, X. In *CCSA 2005, LNCS*; Springer Verlag, Berlin; pp 1083–1092.

[14] Esposito, F.; Capitelli, M.; Gorse, C. *Chem. Phys.* **2000**, *257*, 193 – 202.

[15] Born, M.; Oppenheimer, R. *Ann. Phys. (Leipzig)* **1927**, *84*, 457.

[16] Schwenke, D. *J. Chem. Phys.* **1988**, *89*, 2076.

[17] Bunker, D. L.; Blais, N. C. *J. Chem. Phys.* **1964**, *41*, 2377.

[18] Schwenke, D. *J. Phys. Chem.* **1996**, *100*, 2867.

[19] Schwenke, D. *J. Phys. Chem.* **1996**, *100*, 18884.

[20] Werner, H.-J.; Knowles, P. J. *www.molpro.net*.

[21] R. A. Kendall, J., T. H. Dunning; Harrison, R. J. *J. Chem. Phys.* **1992**, *96*, 6769.

[22] T. H. Dunning, J. *J. Chem. Phys.* **1989**, *90*, 1007.

[23] Wang, D.; Stallcop, J.; Huo, W.; Dateo, C.; Schwenke, D.; Partridge, H. *J. Chem. Phys.* **2003**, *118*, 2186–2189.

[24] Chaban, G.; Jaffe, R.; Schwenke, D.; Huo, W.; *Dissociation Cross Sections and Rate Coefficients for Nitrogen from Accurate Theoretical Calculations*; AIAA Paper AIAA-2008-1209; 2008.

[25] Jaffe, R.; Schwenke, D.; Chaban, G.; *Vibrational and Rotational Excitation and Relaxation of Nitrogen from Accurate Theoretical Calculations*; AIAA Paper AIAA-2008-1208; 2008.

[26] Galvao, B. R. L.; Varandas, A. J. C. *J. Phys. Chem. A* **2009**, *113*, 14424–14430.

[27] Jaffe, R.; Schwenke, D.; Chaban, G.; *Theoretical Analysis of $N_2$ Collisional Dissociation and Rotation-Vibration Energy Transfer*; AIAA Paper AIAA-2009-1569; 2009.

[28] Jaffe, R.; Schwenke, D.; Chaban, G.; *Vibrational and Rotational Excitation and Dissociation in $N_2$-$N_2$ Collisions from Accurate Theoretical Calculations*; AIAA Paper AIAA-2010-4517; 2010.

[29] Paukku, Y.; Yang, K.; Varga, Z.; Truhlar, D. *J. Chem. Phys.* **2013**, *130*, 044309–1:8.

[30] Schwenke, D. W. *J. Chem. Phys.* **2004**, *122*, 14107.

[31] Schwenke, D. W. *Mol. Phys.* **2010**, *108*, 2751.

[32] Le Roy, R.; Huang, Y.; Jary, C. *J. Chem. Phys.* **2006**, *125*, 164310.

[33] LeRoy, R.; Huang, Y.; Jary, C. *J. Phys. Chem.* **2006**, *125*, 164310.

[34] Stallcop, J.; Partrige, H.; Levin, E. *Phys. Rev. A* **2001**, *64*, 042722.

[35] M. Karplus, R. N. P.; Sharma, R. D. *J. Chem. Phys.* **1965**, *43*, 3259–3287.

[36] Taylor, H. S. *Scattering Theory: The Quantum Theory of Nonrelativistic Collisions*; Rober E. Krieger, Malabar, 1983.

[37] Schwenke, D.; Haug, K.; Truhlar, Y., D.J. Sun; Zhang, J.; Kouri, D. *J. Phys. Chem.* **1987**, *91*, 6080.

[38] Schwenke, D.; Haug, K.; Zhao, M.; Truhlar, D.; Sun, Y.; J.Z.H, Z.; Kouri, D. *J. Phys. Chem.* **1988**, *92*, 3202–3216.

[39] McCurdy, C.; Baertschy, M.; Rescigno, T. *J. Phys. B: At. Mol. Opt. Phys.* **2004**, *37*, R137.

[40] Einstein, A. *Ver. Deut. Phys.* **1917**, *19*, 82.

[41] Brillouin, L. *J. Phys.* **1926**, *7*, 353.

[42] Keller, J. *Ann. Phys.* **1958**, *4*, 180.

[43] Goldstein, H. *Classical Mechanics*; Addison-Wesley Publishing Company, Reading, 1980; 2nd edition.

[44] Eaker, C. W. *J. Chem. Phys.* **1989**, *90*, 105–111.

[45] Blais, N. C.; Truhlar, D. G. *J. Chem. Phys.* **1976**, *65*, 5335.

[46] Jaffe, R.; *The Calculation of High-Temperature Equilibrium and Nonequilibrium Specific Heat Data for N−2, O−2 and NO*; AIAA Paper AIAA-1987-1633; 1987.

[47] Cary, B. *Phys. Fluids* **1975**, *8*, 26–35.

[48] Byron, S. *J. Chem. Phys.* **1966**, *44*, 1378–1388.

[49] J. P. Appleton, M. S.; Liquornik, D. *J. Chem. Phys.* **1968**, *48*, 599–608.

[50] Hanson, R. *AIAA J.* **1972**, *10*, 211–215.

[51] Capitelli, M.; Colonna, G.; Esposito, F. *J. Phys. Chem. A* **2004**, *108*, 8930–8934.

[52] Panesi, M.; Jaffe, R. L.; Schwenke, D.; Magin, E. T. *Journal of Chemical Physics* **2013**, *138*, 044312.

[53] Schwenke, D. W. *VKI LS 2008, Non-equilibrium Gas Dynamics* - Rhode-Saint-Genése, Belgium **2008**.

[54] Gear, C. W. *Numerical Initial-Value Problems in Ordinary Differential Equations*; Prentice Hall PTR: Upper Saddle River, NJ, USA, 1971.

[55] Hindmarsh, A. C. *SIGNUM Newsl.* **1980**, *15*, 10–11.

[56] Millikan, R. C.; White, D. R. *J. Chem. Phys.* **1963**, *39*, 3209–3213.

[57] Landau, L.; Teller, E. *Phys. Z. Sowjet.* **1936**, *10*, 34–40.

[58] Landau, L.; Teller, E. *Physik. Z. Sowjetunion* **1937**, *11*, 18.

[59] Robben, F.; Talbot, L. *Phys. Fluids* **1966**, *9*, 633.

[60] Bourdon, A.; Vervish, P. *Phys. Rev. E* **1996**, *54*, 1888–1898.

[61] Panesi, M.; Munafò, A.; Jaffe, R. L.; Magin, T. E. *Phys. Rev. E* **2014**, *90*, 013009.

[62] Munafò, A.; Panesi, M.; Magin, T. E. *Phys. Rev. E* **2014**, *89*, 023001.